Air Force Institute of Technology
AFIT Scholar

Theses and Dissertations | Student Graduate Works

3-2023

Effects of Calibration Errors on Dropped-Channel Polarimetric Synthetic Aperture Radar

Jacob C. Morrison

Follow this and additional works at: https://scholar.afit.edu/etd

 Part of the Electrical and Electronics Commons, and the Signal Processing Commons

Recommended Citation

Morrison, Jacob C., "Effects of Calibration Errors on Dropped-Channel Polarimetric Synthetic Aperture Radar" (2023). *Theses and Dissertations*. 6933.
https://scholar.afit.edu/etd/6933

This Thesis is brought to you for free and open access by the Student Graduate Works at AFIT Scholar. It has been accepted for inclusion in Theses and Dissertations by an authorized administrator of AFIT Scholar. For more information, please contact AFIT.ENWL.Repository@us.af.mil.

Effects of Calibration Errors on Dropped-Channel Polarimetric Synthetic Aperture Radar

THESIS

Jacob C Morrison, Flight Lieutenant, RAAF

AFIT-ENG-MS-23-M-049

DEPARTMENT OF THE AIR FORCE
AIR UNIVERSITY

AIR FORCE INSTITUTE OF TECHNOLOGY

Wright-Patterson Air Force Base, Ohio

DISTRIBUTION STATEMENT A
APPROVED FOR PUBLIC RELEASE; DISTRIBUTION UNLIMITED.

The views expressed in this document are those of the author and do not reflect the official policy or position of the United States Air Force, the United States Department of Defense, United States Government, the Royal Australian Air Force, or any other defence organisation. This material is declared a work of the U.S. Government and is not subject to copyright protection in the United States.

AFIT-ENG-MS-23-M-049

EFFECTS OF CALIBRATION ERRORS ON DROPPED-CHANNEL POLARIMETRIC SYNTHETIC APERTURE RADAR

THESIS

Presented to the Faculty

Department of Electrical and Computer Engineering

Graduate School of Engineering and Management

Air Force Institute of Technology

Air University

Air Education and Training Command

in Partial Fulfillment of the Requirements for the

Degree of Master of Science in Electrical Engineering

Jacob C Morrison, B.S.E.E.

Flight Lieutenant, RAAF

March 23, 2023

DISTRIBUTION STATEMENT A
APPROVED FOR PUBLIC RELEASE; DISTRIBUTION UNLIMITED.

AFIT-ENG-MS-23-M-049

EFFECTS OF CALIBRATION ERRORS ON DROPPED-CHANNEL POLARIMETRIC SYNTHETIC APERTURE RADAR

THESIS

Jacob C Morrison, B.S.E.E.
Flight Lieutenant, RAAF

Committee Membership:

Julie A Jackson, Ph.D
Chair

Richard K Martin, Ph.D
Member

Robert R Mills, Ph.D
Member

Abstract

Compressed Sensing (CS) is a mathematical technique that can be applied to sparse data sets to allow for sub-Nyquist sampling. Dropped-Channel PolSAR Compressive Sensing (DCPCS) is a CS technique that recovers the signal from unmeasured polarisation channels due to antenna crosstalk coupling the information onto the remaining channels. DCPCS reduces data storage/transmission and receiver hardware requirements. This thesis examines the robustness of DCPCS to calibration errors on the antenna crosstalk matrix. Although the antenna design problem is relaxed to a large region of acceptable crosstalk values, very accurate calibration may be required in a monostatic radar. This thesis also looks at the importance of properly setting the basis pursuit denoising (BPDN) threshold ϵ in accordance with the expected clutter and calibration error levels, showing that without any model mismatches it is possible to accurately set ϵ using the estimated scene clutter. Finally, the validity of using a simplified Point Spread Function (PSF) imaging operator to reduce the computational complexity of simulations is shown.

Table of Contents

Page

List of Figures

List of Tables

EFFECTS OF CALIBRATION ERRORS ON DROPPED-CHANNEL POLARIMETRIC SYNTHETIC APERTURE RADAR

I. Introduction

1.1 Problem Background

Synthetic Aperture Radar (SAR) is a key remote sensing technology that is able to provide all-weather day or night imaging, and has important civilian, military, and scientific applications. Polarimetric SAR is an enhanced version of SAR that makes it possible to ascertain additional target information about the reflectors in the scene. The additional information comes at a trade-off of extra data that requires processing, storage and transmission. In recent years, a technique called Compressive Sensing (CS) has been leveraged to attempt to reduce the amount of data required in Polarimetric Synthetic Aperture Radar (PolSAR) systems. Jackson and Lee-Elkin developed a Dropped-Channel PolSAR Compressive Sensing (DCPCS) which uses the inherent polarimetric crosstalk within an antenna to reduce the number of polarisation channels that are required to be measured [1, 2]. Becker has extended the work on DCPCS to show there is a robust design region available over which scene recovery can occur [3,4]. **The goal of this research is to determine the required calibration accuracy of the antenna system in order for DCPCS to be successful. In addition, this thesis will look at the importance of properly setting the basis pursuit denoising (BPDN) threshold ϵ in accordance with the expected noise and calibration error levels.**

1.2 Research Objectives

The research contributions of this work are as follows:

1. Determine the effect of calibration error in the antenna crosstalk model on scene recovery and find a calibration accuracy level required to for successful scene recovery using BPDN for DCPCS.

2. Explore the importance of properly setting the BPDN threshold ϵ with and without model mismatches.

3. Validate the use of simplified imaging operators in place of higher fidelity models to reduce computational loads.

1.3 Document Overview

The remainder of this thesis document is organised as follows. Chapter II presents the relevant background information for the research topics covered and previous work done in the field. Chapter III presents how antenna crosstalk is modelled, the effects of calibration error on the DCPCS model and a recommended antenna calibration level. Chapter IV introduces further research done as part of this thesis to investigate the validity of using simplified imaging operators, the process of setting ℓ_2-norm recovery error threshold, ϵ, in BPDN, and the effects of calibration error on the setting of ϵ. Finally, Chapter V presents the key conclusions from each of the studies, the relevance of the studies, and recommendations for future areas of research.

II. Background and Literature Review

2.1 Chapter Overview

The intent of this chapter is to provide the reader with the necessary information to understand the concepts, results, and conclusions in the following chapters. It is assumed that the reader is familiar with radar and signal processing concepts. The topics discussed in this chapter include Synthetic Aperture Radar (SAR), Compressive Sensing (CS), the Polarimetric Synthetic Aperture Radar (PolSAR) CS model, and antenna calibration.

2.2 Synthetic Aperture Radar

A basic radar operates by transmitting Electromagnetic (EM) energy through an antenna system towards a target. This energy then intercepts the target and is reflected and scattered in all directions. A radar receive antenna (often the same as the transmit) then receives some of the reflected energy. These signals are processed and used to produce a radar output. The size and the shape of the antennas affect the shape of the radar beam and in turn the performance of the radar system as a whole. A larger antenna provides a narrower beamwidth, which in turn yields a finer angular resolution. There are however a number of physical Size, Weight, Power, and Cooling (SWaP-C) constraints that limit the size of antennas used [5].

In 1951 while working for the Goodyear Aircraft company, Carl Wiley invented SAR whilst undertaking work to improve their missile guidance system. [6]. Wiley did not however use the term SAR, he used the terminology of Doppler beam sharpening [7]. SAR is a technique used to generate an artificially large antenna array by using a series of returns from a much smaller antenna that is moving relative to the target. As the SAR platform moves relative to the target the radar transmitter

will periodically transmit pulses and store the returned signals into memory. Each transmission behaves similarly to the elements in an electronic array. At the end of the flight path the receiver will integrate the energy to create a synthetic aperture [5].

SAR radars are used to create radar images of scenes of interest. SAR has the ability to function irrespective of environmental and time factors, making it a key remote sensing technology, critical to military, civilian, and scientific efforts. In the military context SAR images can be used for detection, location, identification, and assessment of targets [8]. Additionally, SAR has applications in agriculture, meteorology, fire management, mapping, and monitoring land subsidence [9].

There are three main types of SAR: strip-map, spotlight, and scanning. In strip-map SAR the antenna maintains a fixed look angle orthogonal to the flight path and sweeps out a large swath on the ground [10]. In spotlight SAR the radar antenna is steered to illuminate a single scene using pulses transmitted from many different viewing angles [7]. In scan SAR the antenna beam is steered to sweep periodically different range sub-swaths to image a larger ground patch than either spotlight or strip-map SAR [11]. Spotlight SAR is the mode of SAR imaging discussed within this thesis. This decision was made in order to maintain consistency with other works in the field [1, 3, 4, 12–14]. Although spotlight SAR is the focus of this thesis, PolSAR CS is compatible with all three types of SAR.

2.2.1 Spotlight SAR

Figure 1 shows the typical airborne spotlight SAR geometry in which the aircraft illuminates a ground patch. The radar looks out the side of the aircraft along the y-axis in Figure 1 in what is known as the range direction. The direction orthogonal to the range is known as the cross-range direction. As the aircraft moves it periodically transmits pulses of microwave energy that interact with targets within the

illuminated patch. Each pulse is then reflected back to the receiver on the aircraft and demodulation procedure is performed. The assembling and preprocessing of data in this fashion generates what is known as phase history data [7]. Phase history is then converted into a SAR image by using an algorithm such as Polar Format Algorthm (PFA) or back projection [15, 16]. However, this thesis will take a linear algebra view of image formation as will be outlined in Section 2.4.1.

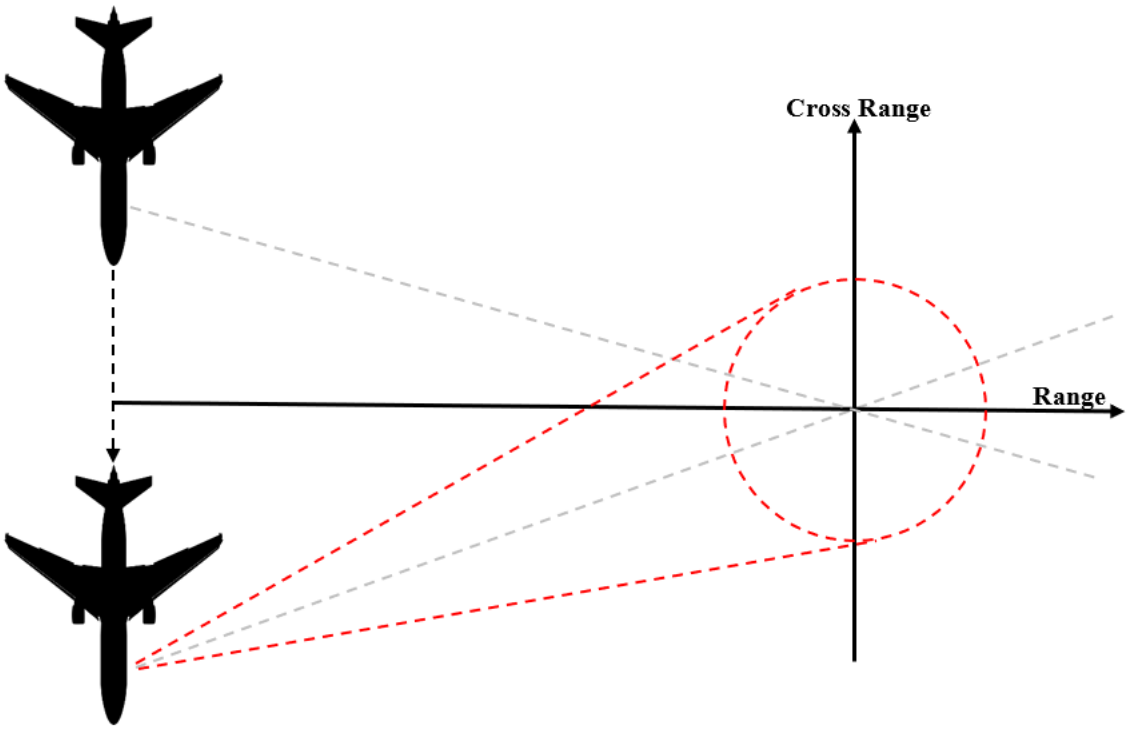

Figure 1: Spotlight Synthetic Aperture Radar Geometry

2.2.2 Polarimetric SAR

Polarimetric SAR (PolSAR) is an enhanced version of SAR in which the radar transmits and receives in multiple polarisations. By utilising different polarisations, it is possible to discern additional information about the reflectors in the target scene. Certain features of a target may provide a stronger return in one polarisation over

another. Thus, by examining the reflection in multiple received channels a more informed picture of the scatterer may be developed. The process of examining multiple polarizations of a target is called polarimetric decomposition [17].

In a dual polarisation system the antenna may transmit and receive either a horizontal (H) or vertical (V) polarised signal. In practice any two orthogonal polarisations are suitable; however, this thesis will only discuss horizontally and vertically polarised signals. PolSAR can be performed by either alternating transmission on multiple polarisations, receiving on multiple polarisations, or both. In the case in which the system both transmits and receives on dual polarisation, there are four received polarisation channels: horizontal transmit - horizontal receive (HH), horizontal transmit - vertical receive (HV), vertical transmit - horizontal receive (VH), and vertical transmit - vertical receive (VV).

A common polarimetric decomposition for radar is the Pauli basis [18]:

$$\boldsymbol{P}_{Pauli} = \frac{1}{\sqrt{2}} \begin{bmatrix} 1 & 1 & 0 & 0 \\ 0 & 0 & 1 & -j \\ 0 & 0 & 1 & j \\ 1 & -1 & 0 & 0 \end{bmatrix} \tag{1}$$

where the first column corresponds to an odd-bounce scatterer and the second column corresponds to even-bounce scatterers (for example, a dihedral with one plate on horizontal ground and the other vertical). A dihedral oriented with its seam rotated 45° about the radar line of sight will result in cross-pol response given by the third column of $\boldsymbol{P}_{Pauli}$ in (1). The fourth column of $\boldsymbol{P}_{\boldsymbol{Pauli}}$ represents a helical scatterer [1]. Each row of (1) corresponds to each of the four polarisation channels listed above (HH, HV, VH, and VV).

The benefits of gathering the extra information of PolSAR however comes with a

cost. SAR imaging already generates large amounts of data that require processing, storage and transmission. The requirements to manage the large amounts of data increase the size, cost, and complexity of the radar system. PolSAR has four times the received data in comparison to regular SAR. Thankfully, sometimes a SAR scene can be represented as sparse in a certain basis. When SAR scenes can be sparsely represented in some basis a technique known as compressed sensing, or compressive sensing [19], can be used to restrict the amount of data that is required to be collected.

2.3 Compressive Sensing

The Shannon-Nyquist sampling theory states that in order to avoid information loss when sampling a signal, samples must be taken at least twice as fast as the signal bandwidth [20]. As the length and/or bandwidth of the signal increases the amount of data required to be collected can rapidly increase. In many applications such as digital cameras the Nyquist rate is so high that the data must be compressed prior to storage or transmission. For applications such Magnetic Resonance Imaging (MRI), radars, and high-speed analogue-to-digital converters, it can become very expensive to increase the sampling rate [21].

The theory of CS, also referred to as compressive sampling or sparse recovery, provides a different technique to data acquisition that allows for sub-Nyquist sampling of certain signals. The goal of compressive sensing is to solve the problem

$$\min_{\boldsymbol{b}} ||\boldsymbol{b}||_0 \text{ s.t. } \boldsymbol{y} = \boldsymbol{A}\boldsymbol{b} \tag{2}$$

where $\boldsymbol{y} \in \mathbb{C}^{M\times 1}$ is observed data, $\boldsymbol{b} \in \mathbb{C}^{N\times 1}$ is the true, unknown scene data, and $\boldsymbol{A} \in \mathbb{C}^{M\times N}$ is an under-determined measurement matrix [22]. The ℓ_0-norm($||\cdot||_0$) is the total number of non-zero entries in a vector. Solving the problem in (2) is

both unstable and NP-Complete meaning that it would be impossible to solve using classical linear algebra techniques. Thankfully, if $\boldsymbol{b}$ is assumed to be sparse then the ℓ_0-norm can be replaced with the ℓ_1-norm($||\cdot||_1$) and sparse signals and closely approximate compressible signals can be recovered [21]. The relaxation to use the ℓ_1-norm produces a basis pursuit (BP) problem of the form

$$\min_{\boldsymbol{b}} ||\boldsymbol{b}||_1 \text{ s.t. } \boldsymbol{y} = \boldsymbol{A}\boldsymbol{b} \tag{3}$$

the ℓ_1-norm is a convex optimisation problem that can be solved using fast and efficient solvers [22]. This research uses a basis pursuit denoising (BPDN) algorithm, which is an extension of the BP technique. The standard form of a BPDN problem is

$$\hat{\boldsymbol{b}} = \arg\min_{\boldsymbol{b}} ||\boldsymbol{b}||_1 \text{ s.t. } ||\tilde{\boldsymbol{y}} - \boldsymbol{A}\boldsymbol{b}||_2 \leq \epsilon, \tag{4}$$

where ϵ is a positive constant that represents a tolerance. By restricting the difference of the ℓ_2-norm of the measured data $\tilde{\boldsymbol{y}}$ and the product $\boldsymbol{A}\boldsymbol{b}$ to be below some tolerance ϵ, BPDN is better positioned to recover signals that have been contaminated by noise than looking for purely the sparsest solution. Appropriate thought must be used when selecting the tolerance level ϵ.

2.3.1 Previous Compressive Sensing in SAR

When applying CS to SAR a designer must consider in which domain(s) the signal is sparse and over which domains they wish to compressively sense. Figure 2 shows that there are three domains that CS techniques can be applied: fast-time range samples, slow-time pulse (or azimuth) samples, and the polarisation receiver channels.

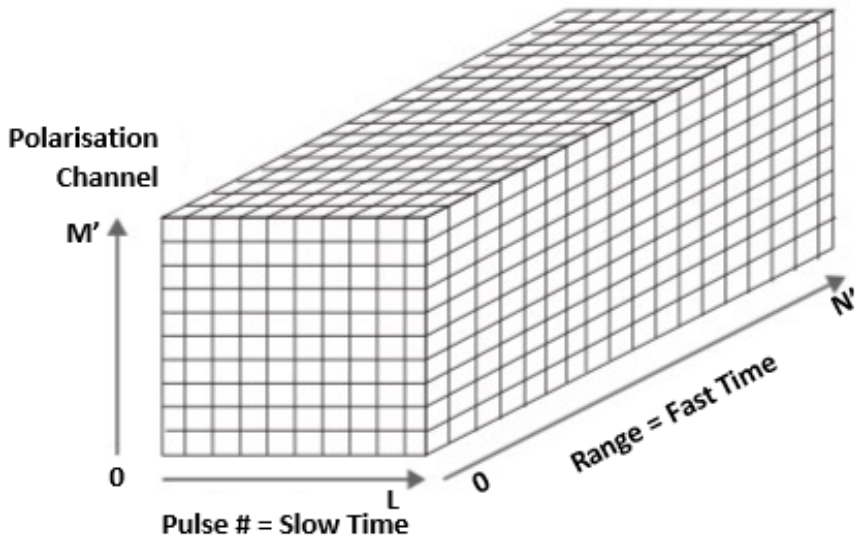

Figure 2: Radar Data Cube

Slow-time CS involves measuring a sub-set of total number of pulses used in the construction of the SAR image. The simplest version of slow-time CS is described in which a random set of azimuth locations are not sampled [23]. Patel et al. suggest a technique of under sampling in the slow-time domain by using a series of random Pulse Repetition Intervals (PRIs). This allows them to measure fewer pulses than regular SAR schemes [24].

Fast time CS involves under-sampling range samples within an individual pulse. There are two main compression schemes that exist that have prototype hardware developed: Xampling ("compressed sampling") and quadrature compressive sampling. Xampling is a system architecture designed for CS for analog inputs whose underlying structure can be modelled as a union of subspaces [25]. The Xampling methodology uses an architecture that includes an analogue-to-digital conversion (ADC) which performs pre-filtering of the signal before taking point-wise low rate samples in order to generate sub-Nyquist Fourier coefficients within certain bands instead of the entire wideband [26]. A non-linear detection algorithm then detects the signal subspace prior to conventional signal processing. Quadrature CS (QuadCS) uses random mod-

ulation by chipping sequence, bandpass filtering, intermediate-frequency sampling and digital quadrature demodulation to collect sub-Nyquist measurements [23, 27].

The polarisation dimension is not typically considered in CS. The next section will describe the scheme proposed by Jackson and Lee-Elkin for PolSAR. The work in Chapters III and IV will concentrate only on PolSAR. In [3] Becker shows that it is possible to combine fast-time, slow-time, and polarimetric compressive sensing into a single model called highly compressed PolSAR.

2.4 Polarimetric Synthetic Aperture Radar Compressive Sensing

Prior to [1], SAR CS was performed on individual receive channels by sub-Nyquist sampling in either the fast and/or slow time domains [24, 26, 28]. In [1, 2] Jackson and Lee-Elkin propose a new CS scheme that allows fully polarimetric SAR imaging while measuring a subset of the polarimetric channels. They call this technique Dropped-Channel PolSAR Compressive Sensing (DCPCS). DCPCS utilises the previously undesirable crosstalk between polarimetric channels that occurs in an antenna to completely recover the information from a channel(s) whose measurements have been dropped. Channel dropping occurs prior to ADC, enabling hardware and computational savings in the receiver.

2.4.1 Dropped-Channel Polarimetric Synthetic Radar Compressive Sensing Model

This section introduces the DCPCS model from [1, 2]. The DCPCS technique proposes measuring M of M' available polarisation channels. Let $\boldsymbol{x_{m'}}$ be an $N' \times 1$ vector of unknown target reflectivity values in $m' = 1, \ldots, M'$ available channels. Let $\boldsymbol{y_m}$ be the corresponding $N \times 1$ vector of observed values for each of the $m = 1, \ldots, M$ measured channels. The observed signal for the mth channel can be represented as

the discrete linear system

$$\boldsymbol{y_m} = \boldsymbol{A_m}(\boldsymbol{x_m} + \boldsymbol{w_m}) \tag{5}$$

for operator $\boldsymbol{A_m}$ and scene clutter vector $\boldsymbol{w_m}$. $\boldsymbol{A_m}$ maps scene reflectivity to measurements, e.g., a range profile, image, or phase history. Other measurement error or noise sources are assumed to be negligible when compared with the scene clutter and are therefore ignored. Expanding (5) for all possible measurement channels $\boldsymbol{y}$ can be expressed as

$$\begin{bmatrix} \boldsymbol{y}_1 \\ \boldsymbol{y}_2 \\ \vdots \\ \boldsymbol{y}_{M'} \end{bmatrix} = \begin{bmatrix} \boldsymbol{A_1} & 0 & 0 & \cdots \\ 0 & \boldsymbol{A_2} & 0 & \\ \vdots & \vdots & \ddots & \vdots \\ 0 & 0 & \dots & \boldsymbol{A_{M'}} \end{bmatrix} \left(\begin{bmatrix} \boldsymbol{x}_1 \\ \boldsymbol{x}_2 \\ \vdots \\ \boldsymbol{x}_{M'} \end{bmatrix} + \begin{bmatrix} \boldsymbol{\omega}_1 \\ \boldsymbol{\omega}_2 \\ \vdots \\ \boldsymbol{\omega}_{M'} \end{bmatrix} \right) \tag{6}$$

which is defined as

$$\boldsymbol{y} = \tilde{\boldsymbol{A}}_{\boldsymbol{M'}}(\boldsymbol{x} + \boldsymbol{w}) \tag{7}$$

where $\boldsymbol{x}, \boldsymbol{w} \in \mathbb{C}^{M'N' \times 1}$. In practice, the observations $\boldsymbol{y}$ have cross-channel coupling, or crosstalk, causing mixing of the reflectivity channels $\boldsymbol{x_{m'}}$ in the observations $\boldsymbol{y_{m'}}$. The ideal block-diagonal structure of $\tilde{\boldsymbol{A}}_{\boldsymbol{M'}}$ does not capture such mixing. To model crosstalk a $M' \times M'$ crosstalk matrix $\boldsymbol{C}$ is defined. Crosstalk matrix $\boldsymbol{C}$ contains coefficients specifying what mixture of the M' pure channels is observed in each of the $1, \dots, M'$ contaminated channels. The Kronecker product ($\otimes$) of the $\boldsymbol{C}$ matrix is taken with a $N' \times N'$ identity matrix, $\boldsymbol{I_{N'}}$, and used to include channel coupling

in (7). Additionally, a $M \times M'$ indicator matrix, $\boldsymbol{J}$, is introduced to represent which channels are measured. $\boldsymbol{J}$ is formed by dropping the unmeasured rows from a $M' \times M'$ identity matrix. This gives the discrete linear system model radar model as

$$\tilde{\boldsymbol{y}} = \tilde{\boldsymbol{A}}_{\boldsymbol{M'}}(\boldsymbol{JC} \otimes \boldsymbol{I}_{N'})(\boldsymbol{x} + \boldsymbol{w}). \tag{8}$$

The scene reflectivity $\boldsymbol{x}$ can be represented by a sparse set of coefficients $\boldsymbol{b}$ in terms of a dictionary $\boldsymbol{D} \in \mathbb{C}^{M'N' \times QS'}$ of scene polarisation responses $\boldsymbol{P} \in \mathbb{C}^{M' \times Q}$ and dictionary of possible spatial responses $\boldsymbol{S} \in \mathbb{C}^{N' \times S'}$. Let the dictionary be

$$\boldsymbol{D} = \boldsymbol{P} \otimes \boldsymbol{S} \tag{9}$$

and define

$$\boldsymbol{A} = \tilde{\boldsymbol{A}}_{\boldsymbol{M}}\text{"}(\boldsymbol{JC} \otimes \boldsymbol{I}_{\boldsymbol{N'}}); \tag{10}$$

then,

$$\tilde{\boldsymbol{y}} = \boldsymbol{ADb} + \boldsymbol{Aw}. \tag{11}$$

For the research in this study the Pauli basis in (1) is used as the polarisation dictionary $\boldsymbol{P}$ and a point target spatial dictionary $\boldsymbol{S}$ is defined by an $N' \times N'$ identity matrix. The CS recovery problem is to solve for a sparse set of coefficients $\boldsymbol{b}$ from measurements $\tilde{\boldsymbol{y}}$. The BPDN problem is

$$\hat{\boldsymbol{b}} = \arg\min_{\boldsymbol{b}} ||\boldsymbol{b}||_1 \text{ s.t. } ||\tilde{\boldsymbol{y}} - \boldsymbol{ADb}||_2 \leq \epsilon. \tag{12}$$

Positive constant ϵ is chosen such that the ℓ_2-norm of the imaged clutter falls within the "error ball" with 95% probability [1].

Using ideal simulations [1] shows that when dropping the HH channel BPDN is able to simultaneously recover the dropped channel, conduct point spread deconvolution and channel de-coupling to generate SAR images of both point and GOTCHA scenes. Jackson and Lee-Elkin also show with point target scenes that objects can be recovered when dropping the two channels that the target responses lie in.

2.4.2 Other Work on DCPCS

Since the introduction of the DCPCS in [1, 2] research into the field has extended the DCPCS model in the following ways: new spatial dictionaries, super-resolution, combining CS techniques, and identification of a robustness region of antenna crosstalk values.

In [29] Becker and Jackson show that the spatial dictionary $\boldsymbol{S}$ in (9) can include any spatial dictionary. Of particular interest they show that by using a spatial dictionary that is well matched to the scatterers in the scene, a sparser representation of the scene can be achieved. In [13] it is shown that the BPDN algorithm is capable of super-resolution of SAR images. Assuming an image pixel is equal in size to a resolution cell, super-resolution seeks to reconstruct an image at a sub-pixel level. The introduction of additional pixels aids in the classification of objects within a scene. Using the measured Air Force Research Laboratory (AFRL) GOTCHA 2006 public data set [30], single and double bounce scattering responses are able to be recovered when a channel has been dropped [13].

In [3] Becker shows that it is possible to combine the fast and slow time CS techniques from Section 2.3.1 with the DCPCS in what he refers to as a "highly compressed PolSAR model". Using the highly compressed PolSAR model he was able to recover a GOTCHA-like scene with a recovery error only approximately 0.14 above baseline while only using 60.75% of the fully sampled data.

Finally, in [3] Becker conducts an analysis on crosstalk levels over which the DCPCS model can provide acceptable recovery performance. The aim of his study is to determine whether there are acceptable system tolerances to facilitate the design and construction of a suitable antenna. Using Monte Carlo trials over random scenes and simulated scenes based on the GOTCHA data set [30] and by employing the BPDN technique, Becker is able to identify a region of crosstalk values that produce acceptable scene recovery.

The primary metric used to evaluate the performance of scene recovery of the BPDN approach is the relative recovery error on $\boldsymbol{b}$ defined as

$$e_b = E\left[\frac{||\boldsymbol{b}_{true} - \hat{\boldsymbol{b}}||_2^2}{||\boldsymbol{b}_{true}||_2^2}\right]. \tag{13}$$

Using three different Point Spread Functions representing aperture sizes of 2.5°, 5°, and 10° to explore across 11 different antenna crosstalk magnitudes, Becker found the relative recovery error of DCPCS for varying antenna designs. Figure 3 is reproduced (with permission) from [3] and shows the average relative recovery, e_b, over 400 Monte Carlo simulations for each of the three antenna apertures and for scenes with sparsities of 1%, 5%, and 10%.

Each of the plots within Figure 3 includes four red dots. The red dots indicate the corners of a region of acceptable robustness. Becker defines the threshold of a successful recovery of an $e_b \leq 0.1$. The 0.1 threshold was chosen based on qualitative

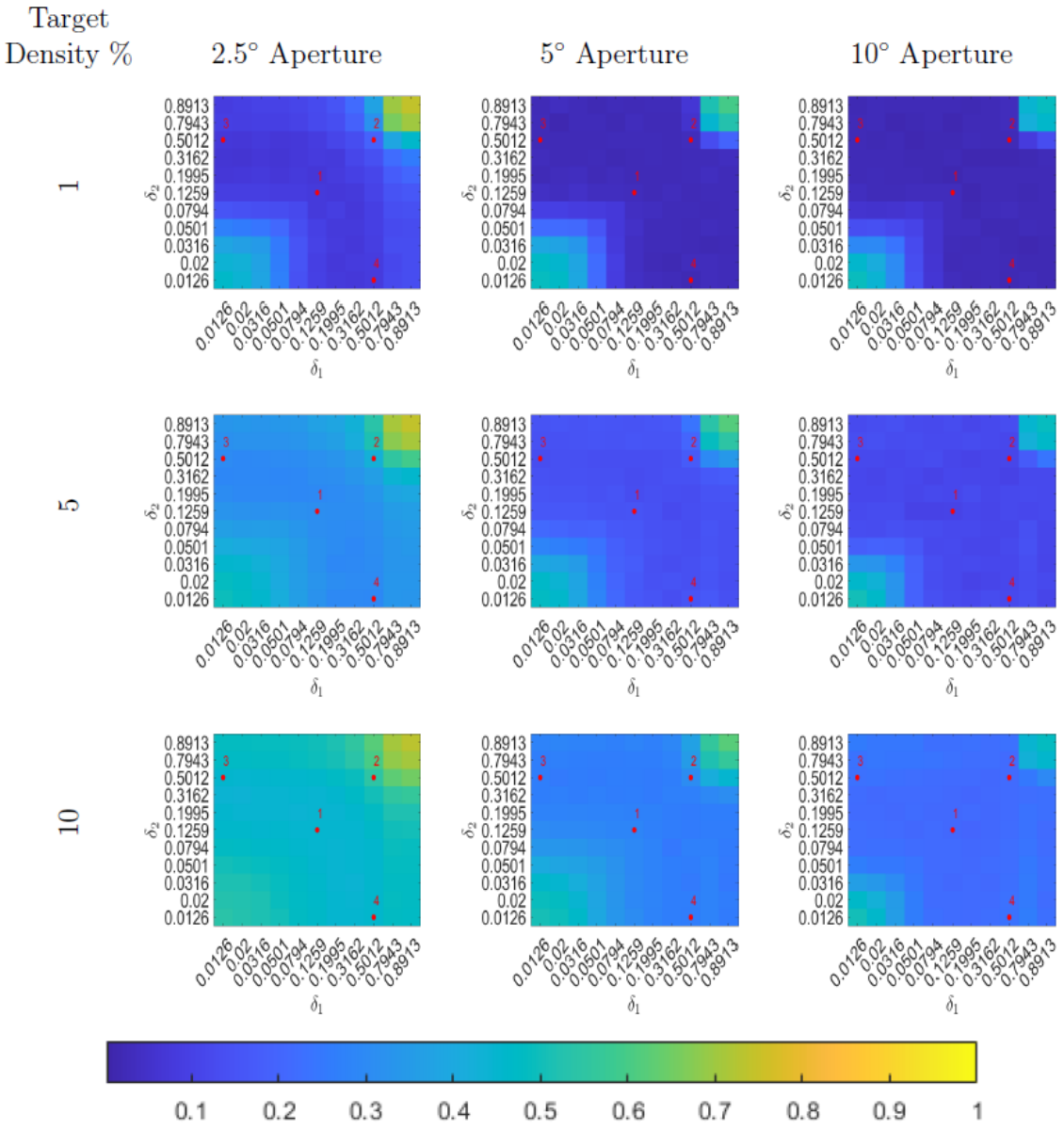

Figure 3: Average of relative recovery error e_b across Monte Carlo Simulations. Target Density levels of 1%, 5%, 10% [3].

observations as the point at which more significant errors such as polarimetric shifts and false positives are seen. Table 1 identifies the crosstalk magnitudes and their average relative recovery performances for each of the four identified corners of the robustness region. Becker also notes that above a 3% scene sparsity, recovery performance degrades above the 0.1 threshold. Figure 3 is defined in terms of crosstalk

parameters δ_1 and δ_2. Crosstalk parameters and how they are used in the DCPCS model are discussed further in Chapter III.

Figure 4 highlights the robustness region identified above on the 2.5° aperture with a 1% sparsity. The corners correspond to crosstalk magnitudes between -18 dB and -6 dB. The identification of such a large robustness region of appropriate crosstalk levels allows for the loosening of antenna design tolerances which in turn enables the practical implementation of the DCPCS method. Unfortunately, these values are much smaller than the typical crosstalk design goals of -30 dB [31]. In order for the DCPCS to work, a novel high crosstalk antenna must be designed and built. In [3, 4] a high crosstalk antenna is designed and constructed and measured. The results from these studies demonstrate sufficient performance of the DCPCS method without sacrificing antenna gain, bandwidth, or radiation pattern. Although Figure 4 indicates small manufacturing errors will not greatly affect BPDN recovery performance of antennas within the red outlined robustness region. However, BPDN recovery also depends on accurate knowledge of the coupling matrix $\boldsymbol{C}$ which is typically gained via system calibration.

Table 1: Crosstalk Pairs to Define Robustness Region [3]

Pair #	δ_1	δ_2	1% Target Density ϵ_b
1	0.1259	0.1259	0.0448
2	0.5012	0.5012	0.0794
3	0.5012	0.0126	0.0381
4	0.0126	0.5012	0.0386

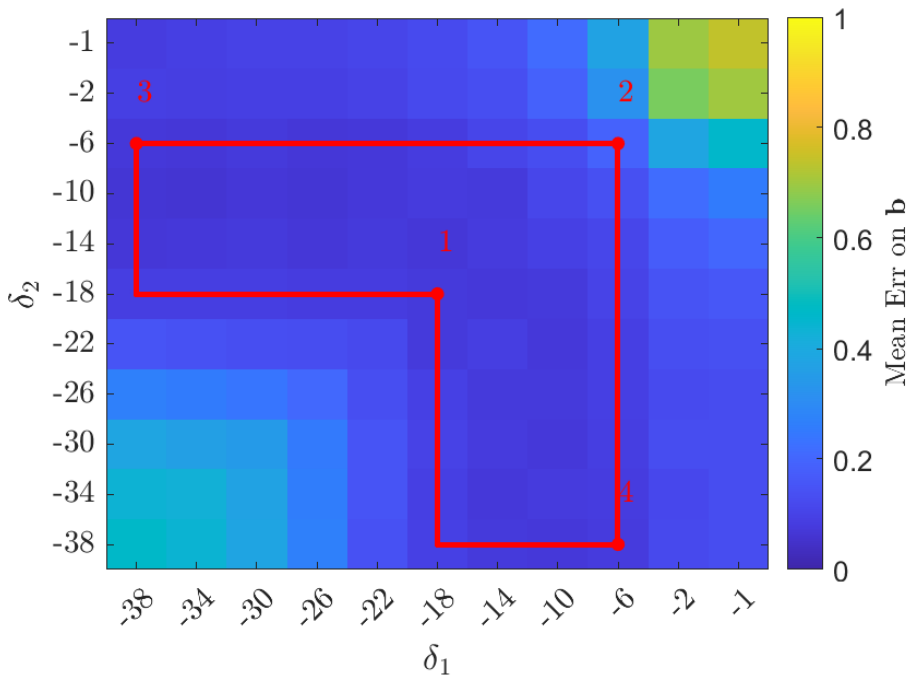

Figure 4: BPDN achieves average relative recovery error e_b less than 0.1 for crosstalk values within the red outline region, corresponding to δ_1 and δ_2 between -18 dB and -6 dB [3].

2.5 Antenna Calibration

Antenna calibration is the process in which the performance of the antenna is verified and the antenna properties are measured. Antenna calibration is important to ensure that repeatable and reliable data is captured from an antenna. There are a number of different antenna properties to consider when calibrating an antenna including: antenna pattern, polarisation, gain, and polarisation crosstalk [32]. In The United States the following standard is used when calibrating an antenna in the near field: ANSI C63.5 - American National Standard for Electromagnetic Compatibility—Radiated Emission Measurements in Electromagentic Interference (EMI) Control—Calibration of Antennas (9 kHz to 40 GHz) [33]. In this thesis the primary element of antenna calibration that we are interested in is the polarisation crosstalk.

III. Robustness of PolSAR CS to Calibration Error

3.1 Chapter Overview

This chapter builds on the concepts introduced in Chapter II and introduces the concepts of antenna crosstalk design. Next, there is a discussion on how Gaussian calibration errors are added to the Dropped-Channel PolSAR Compressive Sensing (DCPCS) from previous studies in order to determine the required radar calibration levels for scene recovery. Finally, the effects of adding different magnitudes of calibration error will be shown empirically through the measure of relative recovery error and implicitly through visual representations of a sample scene.

3.2 Antenna Crosstalk Design

Typical antenna designs seek to minimize cross-channel coupling [34–37]. However, in (11), crosstalk matrix $\boldsymbol{C}$ must be designed such that sufficient mixing of channels occurs to enable basis pursuit denoising (BPDN) recovery of dropped channels. Too much crosstalk will drown out the signal information from the measured channels. Too little crosstalk will not preserve the information from the dropped-channels. Fortunately, as shown in [3, 4], there is a wide range of suitable crosstalk values, enabling much flexibility in the antenna design as well as robustness to manufacturing error.

Crosstalk matrix $\boldsymbol{C}$ captures channel coupling that occurs at both the transmit and receive antenna as well as over the hardware channels. Using the notation from [3],

the transmitter and receiver crosstalk matrices are

$$\boldsymbol{T} = \begin{bmatrix} \frac{t_{HH}}{\sqrt{|t_{HH}|^2+|\delta_1|^2}} & \frac{\delta_1}{\sqrt{|t_{HH}|^2+|\delta_1|^2}} \\ \frac{\delta_2}{\sqrt{|t_{VV}|^2+|\delta_2|^2}} & \frac{t_{VV}}{\sqrt{|t_{VV}|^2+|\delta_2|^2}} \end{bmatrix} \tag{14}$$

$$\boldsymbol{R} = \begin{bmatrix} \frac{r_{HH}}{\sqrt{|r_{HH}|^2+|\delta_3|^2}} & \frac{\delta_3}{\sqrt{|r_{HH}|^2+|\delta_3|^2}} \\ \frac{\delta_4}{\sqrt{|r_{VV}|^2+|\delta_4|^2}} & \frac{r_{VV}}{\sqrt{|r_{VV}|^2+|\delta_4|^2}} \end{bmatrix} \tag{15}$$

where $\delta_i, i \in [1,2,3,4]$ are crosstalk parameters. The total power of each row of (14)-(15) is normalised to one to ensure conservation of power in the system. A linear polarization basis with H horizontal and V vertical is assumed, though other polarization bases may be used. The total system crosstalk is

$$\boldsymbol{C} = \boldsymbol{T} \otimes \boldsymbol{R}^T \tag{16}$$

$$= \begin{bmatrix} o\frac{t_{HH}}{\sqrt{|t_{HH}|^2+|\delta_1|^2}} & \frac{\delta_1}{\sqrt{|t_{HH}|^2+|\delta_1|^2}} \\ \frac{\delta_2}{\sqrt{|t_{VV}|^2+|\delta_2|^2}} & \frac{t_{VV}}{\sqrt{|t_{VV}|^2+|\delta_2|^2}} \end{bmatrix} \otimes \begin{bmatrix} \frac{r_{HH}}{\sqrt{|r_{HH}|^2+|\delta_3|^2}} & \frac{\delta_3}{\sqrt{|r_{HH}|^2+|\delta_3|^2}} \\ \frac{\delta_4}{\sqrt{|r_{VV}|^2+|\delta_4|^2}} & \frac{r_{VV}}{\sqrt{|r_{VV}|^2+|\delta_4|^2}} \end{bmatrix}^T \tag{17}$$

If we assume a monostatic radar (17) can be simplified to

$$\boldsymbol{C} = \boldsymbol{T} \otimes \boldsymbol{T}^T \tag{18}$$

$$= \begin{bmatrix} \frac{t_{HH}}{\sqrt{|t_{HH}|^2+|\delta_1|^2}} & \frac{\delta_1}{\sqrt{|t_{HH}|^2+|\delta_1|^2}} \\ \frac{\delta_2}{\sqrt{|t_{VV}|^2+|\delta_2|^2}} & \frac{t_{VV}}{\sqrt{|t_{VV}|^2+|\delta_2|^2}} \end{bmatrix} \otimes \begin{bmatrix} \frac{t_{HH}}{\sqrt{|t_{HH}|^2+|\delta_1|^2}} & \frac{\delta_1}{\sqrt{|t_{HH}|^2+|\delta_1|^2}} \\ \frac{\delta_2}{\sqrt{|t_{VV}|^2+|\delta_2|^2}} & \frac{t_{VV}}{\sqrt{|t_{VV}|^2+|\delta_2|^2}} \end{bmatrix}^T \tag{19}$$

$$= \begin{bmatrix} \frac{t_{HH}^2}{\mathbf{t}_1^2} & \frac{\delta_2}{\mathbf{t}_2}\frac{t_{HH}}{\mathbf{t}_1} & \frac{\delta_1 t_{HH}}{\mathbf{t}_1^2} & \frac{\delta_1}{\mathbf{t}_1}\frac{\delta_2}{\mathbf{t}_2} \\ \frac{\delta_1 t_{HH}}{\mathbf{t}_1^2} & \frac{t_{HH}}{\mathbf{t}_1}\frac{t_{VV}}{\mathbf{t}_2} & \frac{\delta_1^2}{\mathbf{t}_1^2} & \frac{\delta_1}{\mathbf{t}_1}\frac{t_{VV}}{\mathbf{t}_2} \\ \frac{t_{HH}}{\mathbf{t}_1}\frac{\delta_2}{\mathbf{t}_2} & \frac{\delta_2^2}{\mathbf{t}_2^2} & \frac{t_{HH}}{\mathbf{t}_1}\frac{t_{VV}}{\mathbf{t}_2} & \frac{\delta_2 t_{VV}}{\mathbf{t}_2^2} \\ \frac{\delta_1}{\mathbf{t}_1}\frac{\delta_2}{\mathbf{t}_2} & \frac{\delta_2 t_{VV}}{\mathbf{t}_2^2} & \frac{\delta_1}{\mathbf{t}_1}\frac{t_{VV}}{\mathbf{t}_2} & \frac{t_{VV}^2}{\mathbf{t}_2^2} \end{bmatrix} \tag{20}$$

where $\mathbf{t_1} = \sqrt{|t_{HH}|^2 + |\delta_1|^2}$ and $\mathbf{t_2} = \sqrt{|t_{VV}|^2 + |\delta_2|^2}$. The columns and rows of $\boldsymbol{C}$ represent the polarisation channels (HH, HV, VH, and VV) in the reflectivity and measurement domains, respectively. The elements along the diagonal represent the signal response in each channel, and the off-diagonal entries represent the channel crosstalk. For example, the first row of $\boldsymbol{C}$ represents data on the HH channel and data from the HV, VH, and VV channels that are mixed into the HH measurement. The values in $\boldsymbol{C}$ may be complex to capture both the magnitude and phase of the crosstalk behaviour. As in [1, 3], we assume for simplicity that the coupling is not dependent on frequency, time, or angle.

In [3] Becker found the region of crosstalk parameters in which acceptable scene recovery occurs. The points that represent the corners of Becker's crosstalk robustness region are listed in Table 1. To produce the transmit/receive crosstalk matrices for Points 1-4 shown in Figure 4, set $t_{HH} = t_{VV} = 1$ and use the δ_i values shown in the Table 1. The four normalised matrices are [3]

$$\boldsymbol{T}_1 = \boldsymbol{R}_1 = \begin{bmatrix} 0.9922 & 0.1249 \\ 0.1249 & 0.9922 \end{bmatrix} \tag{21}$$

$$\boldsymbol{T}_2 = \boldsymbol{R}_2 = \begin{bmatrix} 0.8940 & 0.4481 \\ 0.4481 & 0.8940 \end{bmatrix} \tag{22}$$

$$\boldsymbol{T}_3 = \boldsymbol{R}_3 = \begin{bmatrix} 0.9999 & 0.0126 \\ 0.4481 & 0.8940 \end{bmatrix} \tag{23}$$

$$\boldsymbol{T}_4 = \boldsymbol{R}_4 = \begin{bmatrix} 0.8940 & 0.4481 \\ 0.0126 & 0.9999 \end{bmatrix}. \tag{24}$$

In [4] a high crosstalk S-band patch antenna is designed, with design goal of Point

2 ($\delta_1 = \delta_2 = 0.5012 = -6$ dB) in Figure 4. After calibration and measurement using principle plane analysis, the antenna crosstalk is

$$\boldsymbol{T}_{\text{meas}} = \boldsymbol{R}_{\text{meas}} = \begin{bmatrix} 0.6169 - 0.5287i & 0.5830 + 0.0001i \\ 0.7028 + 0.5039i & 0.5016 + 0.0245i \end{bmatrix} \tag{25}$$

The measured crosstalks are $\delta_1 = -1.4404$ dB and $\delta_2 = -2.3606$ dB at the centre frequency. Despite higher than desired crosstalk, examples in [4] and Section 3.4 indicate sufficient BPDN recovery performance is possible. The crosstalk phase aids recovery compared to the real-valued crosstalk matrices in Figure 4 [3]. These five crosstalk matrices (21)-(25) will form the basis of the monostatic radars that will be evaluated throughout the remainder of this thesis.

Results in [3,12] indicate improved recovery can be achieved by using two different antennas (with different crosstalk values) for transmit and receive. One such crosstalk pair that resulted in reasonable recovery results for a Pauli polarisation dictionary are the crosstalk matrices from [1]:

$$\begin{aligned} \boldsymbol{T}_{\text{Jackson}} &= 0.78 \begin{bmatrix} 1 & 0.8\underline{/3.03} \\ 0.91\underline{/0.29} & 0.91 \end{bmatrix} \\ &= \begin{bmatrix} 0.78 & -0.62 + j0.07 \\ 0.68 + j0.20 & 0.71 \end{bmatrix} \end{aligned} \tag{26}$$

$$\begin{aligned} \boldsymbol{R}_{\text{Jackson}} &= 0.93 \begin{bmatrix} 1 & 0.4\underline{/-1.63} \\ 0.4\underline{/-1.63} & 1 \end{bmatrix} \\ &= \begin{bmatrix} 0.93 & -0.02 - j0.37 \\ -0.02 - j0.37 & 0.93 \end{bmatrix}. \end{aligned} \tag{27}$$

Crosstalk matrices (26) and (27) were arbitrarily selected and do not exactly follow the δ_i format defined in (14) and (15). Crosstalk (26) and (27) correspond to $|\delta_1| \approx 0.8|t_{HH}|$, $|\delta_2| \approx |t_{VV}|$, $|\delta_3| \approx 0.4|r_{HH}|$, and $|\delta_4| \approx 0.4|r_{VV}|$. Plugging in values of $t_{HH} = t_{VV} = 1$ as in (21)-(24) yields crosstalk values of approximately 0.4 to 0.8, which are inside or near the upper right corner of the outlined robustness region.

3.3 Introduction of Calibration Error

In all previous DCPCS research, *a priori* knowledge of the crosstalk matrix has been assumed. In practice, the true values are known only within the uncertainty of the antenna measurement/calibration equipment. Even accurate pre-flight calibration can drift during radar operation due to vibrations or thermal drift [38]. Crosstalk model inaccuracy leads to inaccuracy in the signal mapping matrix $\boldsymbol{A}$ (10) used in BPDN recovery (12). Here and in [14], we introduce calibration error to the system by adding independent, identically distributed complex white Gaussian noise to each of the four terms in $\boldsymbol{T}$ and $\boldsymbol{R}$. Modeling error in this fashion assumes the same measurement equipment is used for calibration of both the co-pol and cross-pol channels. A Gaussian distribution of errors is supported by [39] reporting their errors as the standard deviation of the calibration accuracy of the radar system.

Let the calibration error terms $\boldsymbol{\Delta}_T$ and $\boldsymbol{\Delta}_R$ be 2×2 matrices with each element distributed as $\sim \mathcal{CN}(0, \sigma_{\text{err}}^2)$. The resulting matrix is re-normalized such that the measured antenna matrix representation obeys conservation of power laws. Then, the measured crosstalk matrix $\hat{\boldsymbol{C}}$ is represented as

$$\hat{\boldsymbol{C}} = \left(\widehat{\boldsymbol{T} + \boldsymbol{\Delta}_T}\right) \otimes \left(\widehat{\boldsymbol{R} + \boldsymbol{\Delta}_R}\right)^T \tag{28}$$

where the wide hat notation indicates the normalization of matrix rows. For the

single antenna, monostatic case, the same error realisation ($\boldsymbol{\Delta}_R = \boldsymbol{\Delta}_T$) is added to both the transmit and receive crosstalk matrices. Although this study considers a $\boldsymbol{C}$ that is not dependent on frequency or angle, such variations could be thought of as calibration error in a particular snapshot.

If the measured crosstalk $\hat{\boldsymbol{C}}$ is used in place of the true crosstalk in the measurement model, then the $\boldsymbol{A}$ matrix becomes

$$\hat{\boldsymbol{A}} = \tilde{\boldsymbol{A}}_M(\boldsymbol{J}\hat{\boldsymbol{C}} \otimes \boldsymbol{I}_{N'}) \tag{29}$$

Furthermore, using the measured crosstalk $\hat{\boldsymbol{C}}$ for BPDN recovery yields

$$\hat{\boldsymbol{b}} = \arg\min_{\boldsymbol{b}} ||\boldsymbol{b}||_1 \text{ s.t. } ||\tilde{\boldsymbol{y}} - \hat{\boldsymbol{A}}\boldsymbol{D}\boldsymbol{b}||_2 \leq \epsilon. \tag{30}$$

The ℓ_2 fit is impaired by both the measured clutter $\boldsymbol{A}\boldsymbol{w}$ and model mismatch $\boldsymbol{A} - \hat{\boldsymbol{A}}$:

$$||\tilde{\boldsymbol{y}} - \hat{\boldsymbol{A}}\boldsymbol{D}\boldsymbol{b}||_2 = ||(\boldsymbol{A} - \hat{\boldsymbol{A}})\boldsymbol{D}\boldsymbol{b} + \boldsymbol{A}\boldsymbol{w}||_2 \tag{31}$$

In the next section, we show BPDN recovery results as a function of calibration error variance σ^2_{err}. The ℓ_2 radius ϵ is set according to the clutter, as in previous work, since the model mismatch term in (31) depends on the unknown coefficients $\boldsymbol{b}$. Forcing ℓ_2 fit may increase the ℓ_1 norm of solution $\hat{\boldsymbol{b}}$, potentially increasing relative recovery error e_b. Thus, the following analysis is somewhat pessimistic. In Chapter IV epsilon setting in the face of calibration errors is discussed and the appropriateness of relaxing ϵ is explored.

3.4 Results

In order to investigate the effects of calibration errors on relative recovery error, simulations of a small 5×5 pixel point target scene are randomly generated. The results of this study will inform us on the resilience of DCPCS to calibration errors. The crosstalk matrix $\boldsymbol{C}$ used in the experiment is formed using the various crosstalk designs from Section 3.2 in Equations (21)-(27). The measured crosstalk $\hat{\boldsymbol{C}}$ used in BPDN recovery is generated as described in Section 3.1, and solved using the *spgl1* algorithm [40,41], with the calibration error variance σ_{err}^2. The Point Spread Function (PSF) used in the construction of the image formation operator $\tilde{\boldsymbol{A}}_M$ is the simplified PSF from [1]:

$$\text{PSF} = \begin{bmatrix} 0 & 0.5 & 0 \\ 0.5 & 1 & 0.5 \\ 0 & 0.5 & 0 \end{bmatrix};$$

the mth block of $\tilde{\boldsymbol{A}}_M$ is a two-dimensional convolution of the scene reflectivity in the mth polarisation channel with the PSF. Although the simplified PSF was not used in the study that the crosstalk matrices were developed, Chapter IV will show that it is valid to make this substitution. The target dictionary $\boldsymbol{D}$ is comprised of the Pauli polarisation basis $\boldsymbol{P}$ (1) and a point target spatial dictionary $\boldsymbol{S} = \boldsymbol{I}$. Target dictionary coefficients $\boldsymbol{b}$ are randomly set to zero or one according to the desired sparsity. The HH channel is chosen as the channel to be dropped.

Figures 5 and 6 show an example scene with sparsity of 3%, signal to clutter ratio SCR=40 dB, and varying levels of calibration error for crosstalk matrices $\boldsymbol{C} = \boldsymbol{T}_2 \otimes \boldsymbol{T}_2^T$ and $\boldsymbol{C} = \boldsymbol{T}_{\text{Jackson}} \otimes \boldsymbol{R}_{\text{Jackson}}^T$, respectively. The pixels in the scene are numbered from top to bottom and from left to right. The scene consists of an even bounce reflected in the 7th pixel location, which has half its reflected energy in the horizontal plane and half in the vertical plane, and an object in the 19th pixel location with a purely

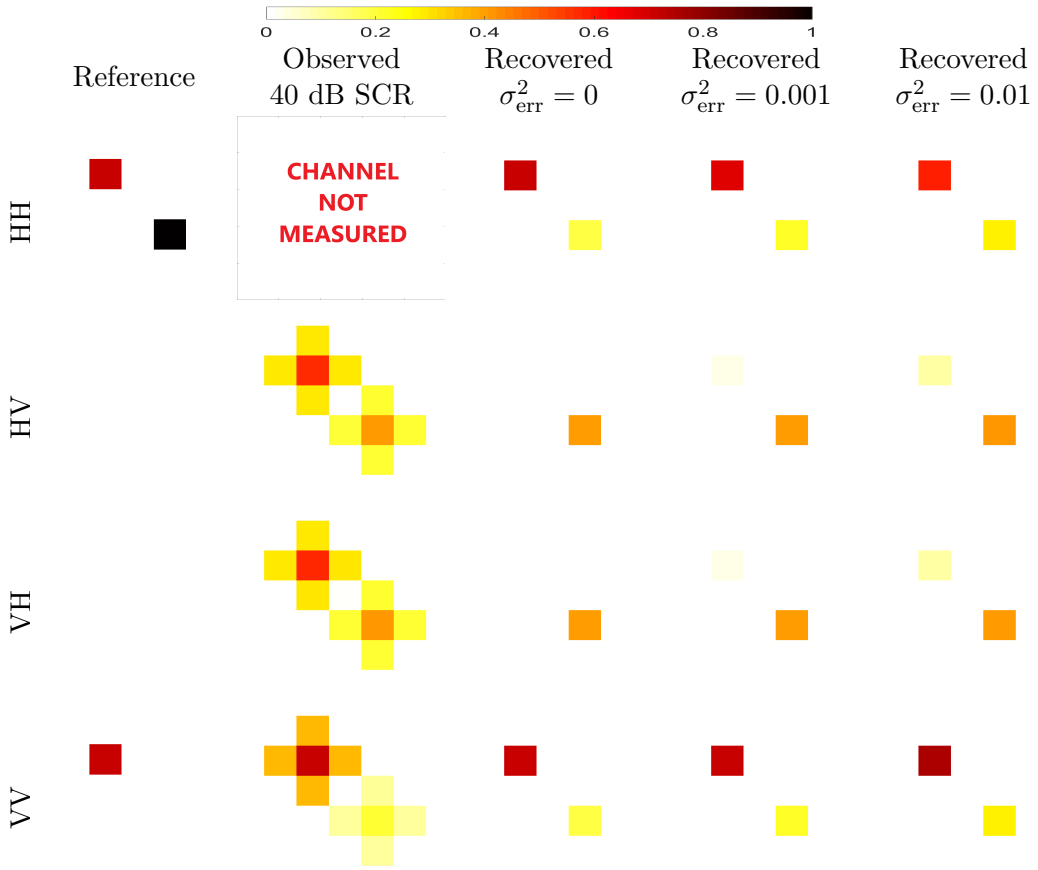

Figure 5: Reference, Observed, and Recovered images of point targets at 40 dB SCR, using crosstalk $\boldsymbol{C} = \boldsymbol{T}_2 \otimes \boldsymbol{T}_2^T$ and calibration errors of $\sigma^2_{\text{err}} = 0, 0.001,$ and 0.01.

horizontal plane return.

In Figure 5, the PSF can be clearly seen in all three of the observed measurement channels. The dropped channel is mostly recovered, and all the channels are unmixed to some degree. However, the high levels of crosstalk present in the antenna make it difficult for the BPDN algorithm to determine whether the object in the 19th pixel is a cross talk artifact or not. The introduction of calibration error appears to have had very minimal effect on the recovered scene at a level of $\sigma^2_{err} = 0.001$. Additional false returns begin to be faintly visible at $\sigma^2_{err} = 0.01$.

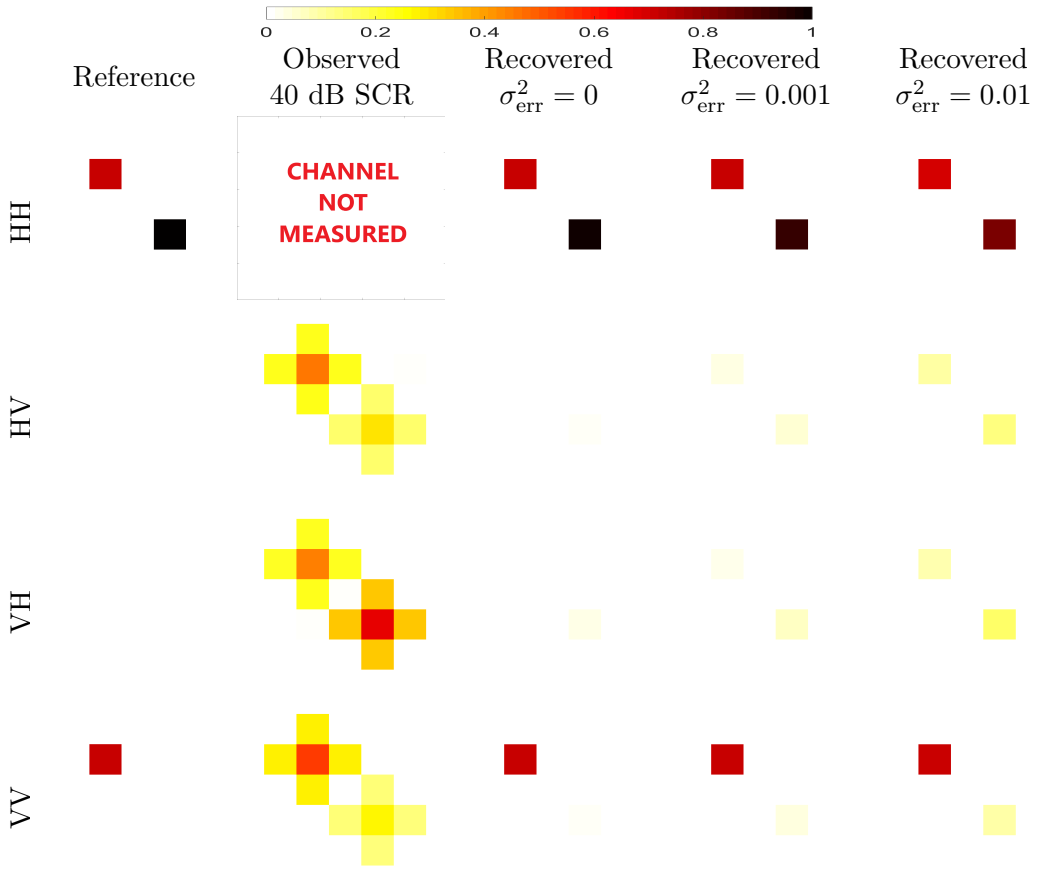

Figure 6: Reference, Observed, and Recovered images of point targets at 40 dB SCR, using crosstalk $\boldsymbol{C} = \boldsymbol{T}_{\text{Jackson}} \otimes \boldsymbol{R}^T_{\text{Jackson}}$ and calibration errors of $\sigma^2_{\text{err}} = 0, 0.001, \text{and } 0.01$.

Figure 6 again shows the PSF in the observed measured signals. The Jackson antennas have near perfect scene recovery even in the presence of calibration errors. There are faint artifacts visible in the co-pol channels at higher calibration error levels but the magnitude of these returns are approximately five times fainter than the weakest true return.

The remainder of this section analyses random scenes to more fully characterize performance recovery for different crosstalk matrices as a function of scene sparsity, Signal-to-Clutter Ratio (SCR), and calibration error variance σ^2_{err}.

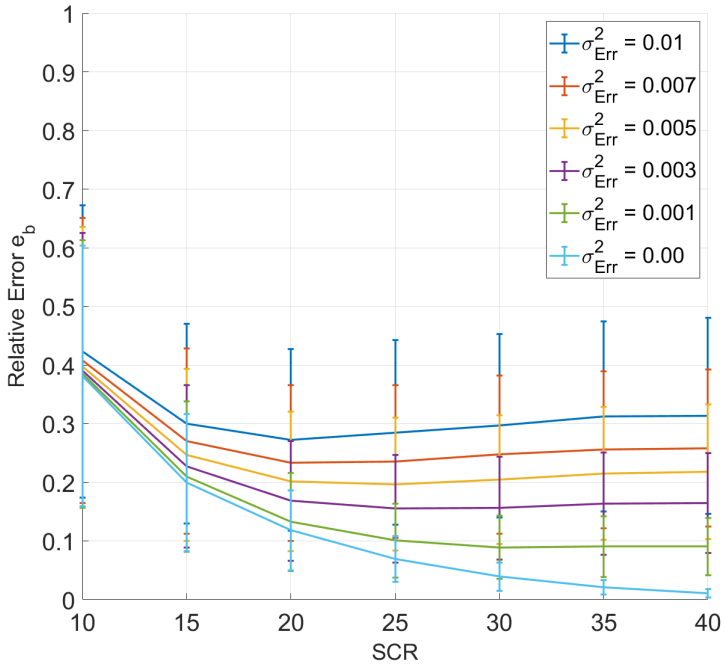

Figure 7: Median Relative Error versus SCR for sparsity = 0.01 and crosstalk $\boldsymbol{C} = \boldsymbol{T}_{\text{meas}} \otimes \boldsymbol{T}_{\text{meas}}^{T}$. HH Channel dropped. Error bars indicate the 10th and 90th percentiles.

Monte Carlo trials are conducted on 100 randomly generated scenes (draws of $\boldsymbol{b}$) and 100 random draws of calibration error $\boldsymbol{\Delta}_T$, $\boldsymbol{\Delta}_R$, resulting in 10,000 trials per parameter set. Figure 7 shows the median relative error (replace mean operator E with median in (13)) versus SCR for various amounts of calibration error on the measured antenna values in (25). The scene sparsity is 1%, and the HH channel is dropped. As the SCR increases the relative error decreases, indicating a higher quality image recovery. In [3,4] $e_b < 0.1$ is selected as a "successful recovery" threshold, above which it is qualitatively observed that more visually significant errors begin to occur. This ($e_b < 0.1$) is the threshold that will be used for the remainder of the thesis. In Figure 7, successful recovery ($e_b < 0.1$) is achieved for moderate to high SCRs for calibration errors less than $\sigma^2_{\text{err}} < 0.001$. Thus, antenna crosstalk calibration error less than -30 dB is desired for the high crosstalk antenna T_{meas} (25).

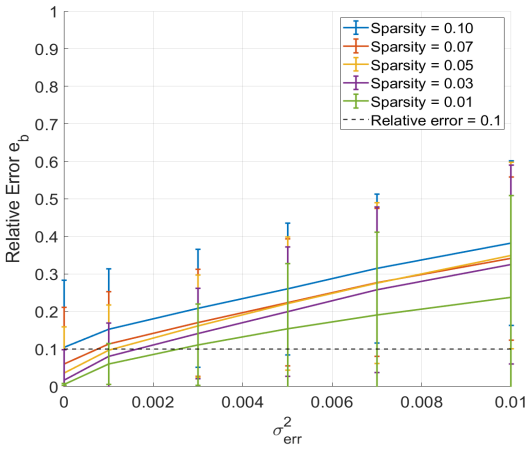

(a) $\boldsymbol{C} = \boldsymbol{T}_1 \otimes \boldsymbol{T}_1^T$

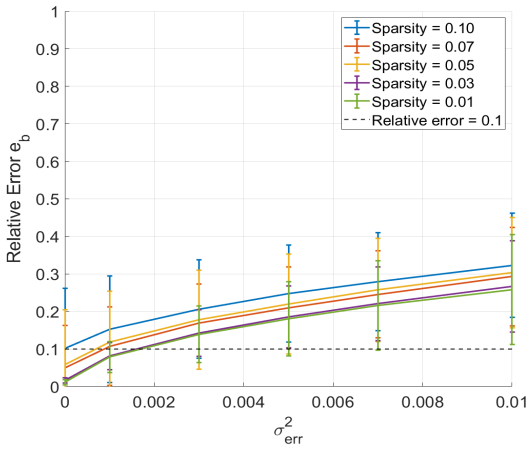

(b) $\boldsymbol{C} = \boldsymbol{T}_2 \otimes \boldsymbol{T}_2^T$

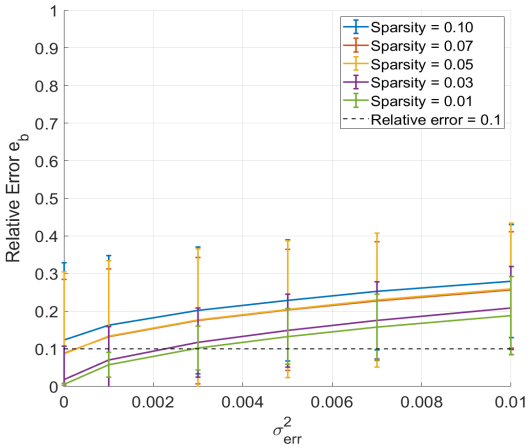

(c) $\boldsymbol{C} = \boldsymbol{T}_3 \otimes \boldsymbol{T}_3^T$

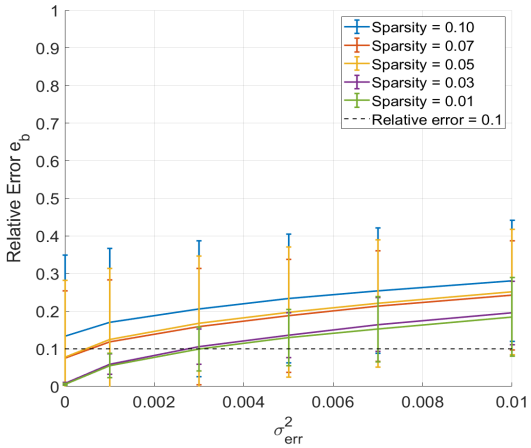

(d) $\boldsymbol{C} = \boldsymbol{T}_4 \otimes \boldsymbol{T}_4^T$

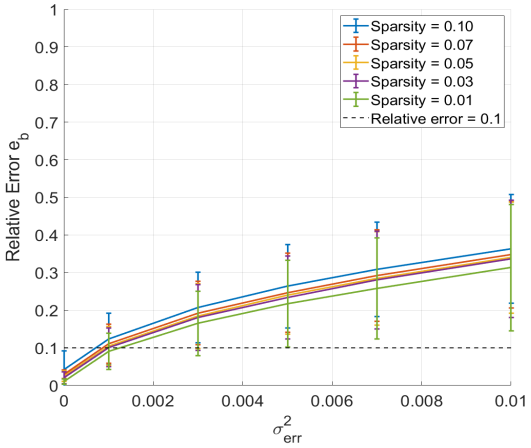

(e) $\boldsymbol{C} = \boldsymbol{T}_{\text{meas}} \otimes \boldsymbol{T}_{\text{meas}}^T$

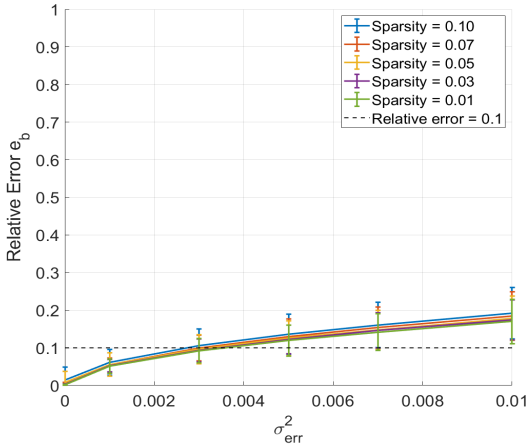

(f) $\boldsymbol{C} = \boldsymbol{T}_{\text{Jackson}} \otimes \boldsymbol{R}_{\text{Jackson}}^T$

Figure 8: Median relative error versus calibration error σ_e^2 for SCR = 40 dB and HH channel dropped for crosstalks (21)-(27). Error bars indicate the 10th and 90th percentiles.

Table 2: Calibration accuracy required for succesful recovery ($e_b < 0.1$) with SCR=40 dB and 1% sparsity (best case scenario)

Antenna	$\boldsymbol{T}_1$	$\boldsymbol{T}_2$	$\boldsymbol{T}_3$	$\boldsymbol{T}_4$	$\boldsymbol{T}_{meas}$	$\boldsymbol{T}_{Jackson}$
$10\log_{10}\sigma^2_{err}$ (dB)	-25.9	-27.7	-25.4	-25.2	-29.0	-24.6

Figures 8a-8f show the median relative error versus the calibration error for the crosstalk antennas in (21)-(27). Sparsity is varied, and SCR is 40 dB. A slight difference in imaging operators results in a small difference in relative error when $\sigma^2_{err} = 0$ as compared to [3]; however, the trends are similar. Recovery error increases as both calibration error and scene target density (sparsity value) increase. Figures 8a-8d indicate that calibration accuracy to achieve $e_b < 0.1$ should be approximately $\sigma^2_{\text{err}} < 0.003$ for sparse scenes or $\sigma^2_{\text{err}} < 0.002$ for less sparse scenes, corresponding to -25 dB and -27 dB antenna calibration error standard deviation. Antenna T_{meas} is outside of the robustness region, so recovery performance and required calibration error is on average slightly worse than for T_2; however the phase crosstalk in T_{meas} makes its performance less variable. The curves in Figure 8f show $\boldsymbol{C} = \boldsymbol{T}_{\text{Jackson}} \otimes \boldsymbol{R}^T_{\text{Jackson}}$ is more robust to calibration error than the single antenna crosstalk's tested. Using separate antennas for transmit and receive improves performance and can relax the calibration requirement to $\sigma^2_{\text{err}} < 0.003$ (calibration error -25 dB) for all sparsities; optimizing the design of the $\boldsymbol{T}$ and $\boldsymbol{R}$ combination could further improve results.

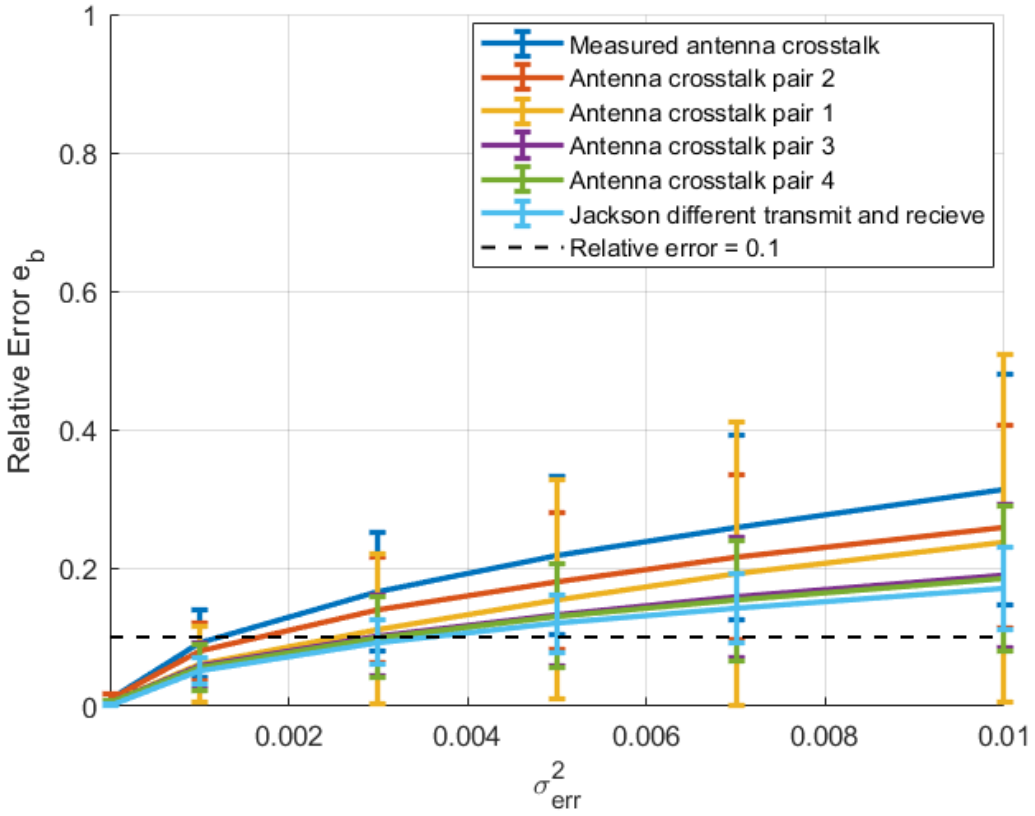

Figure 9: Median Relative Error versus calibration error for 1% sparsity and SCR=40 dB. Comparison of different antenna designs. HH channel dropped. Errors bars indicate the 10th and 90th percentiles.

Figure 9 compares the six different antennas for the best case scenario of $SCR = 40\ dB$ and 1% scene sparsity. Interpolating the data in Figure 9 the calibration accuracy required to achieve successful recovery $e_b < 0.1$ is approximately -25 dB for all of the antennas except T_2 and T_{meas}; values for each antenna are listed in Table 2. Reduced performance of T_2 and T_{meas} is expected from Figure 4, as Design Point 2 error is more than twice that of points within the robustness region, and T_{meas} lies outside the robustness region toward the upper right. Thus, improved performance and a more relaxed calibration requirement can be achieved by using Design Points 1, 3, 4, or others within the robustness region. The dual antenna case generally outperforms all of the single antenna design points, though the calibration

requirement is approximately the same.

3.5 Conclusions

We have shown that radar calibration accuracy on the order of -25 dB or better is needed for successful recovery of scenes using BPDN for DCPCS in a single antenna system. However, there is room for improvement. The use of separate antennas for transmit and receive improves recovery; such designs should be studied further. Also, as noted in Section 3.3 relaxation of the ℓ_2 fit setting ϵ may improve recovery and will be further explored in Chapter IV. Finally, it should be studied whether self-calibration methods such as [42, 43] that estimate unknowns in the $\boldsymbol{A}$ matrix in addition to estimating $\boldsymbol{b}$ can overcome limitations in calibration measurement accuracy.

IV. Further investigations

4.1 Section Overview

This chapter builds on the concepts introduced in Chapter II and offers an expansion on some topics identified in Chapter III. First, the effects of using a simplified imaging operator in the modelling of calibration error will be explored. This will tie in neatly with previous work done by Becker in [3]. We will then introduce the math behind setting the ϵ value to account for scene clutter. Finally, we investigate how the introduction of calibration error may necessitate and adjustment to the setting of ϵ due to effects of model mismatches contributing to residual error.

4.2 Change of Imaging Operator

4.2.1 Section Overview

Synthetic Aperture Radar (SAR) images can be thought of as the output of the imaging operator performed on the scene reflectivity to produce measurements in the form of a range profile, image, or phase history [44]. Spotlight SAR image formation can be thought of as the convolution of the scene reflectivity and the Point Spread Function (PSF) of the radar in the image domain. A PSF takes the form of a two-dimensional sinc function. The shape of the sinc is defined by the aperture extent in the cross-range direction and by the radar bandwidth in the range direction. Examples of PSFs with 2.5°, 5.0°, and 10° aperture extents from [3] can be seen in Figure 10.

Figure 10 demonstrates that by increasing the aperture extent of the radar system, a much narrower PSF can be achieved. It can be clearly understood that by convolving these three different PSF with the same scene reflectivity will result in three different sets of measured data. In the Dropped-Channel PolSAR Compressive

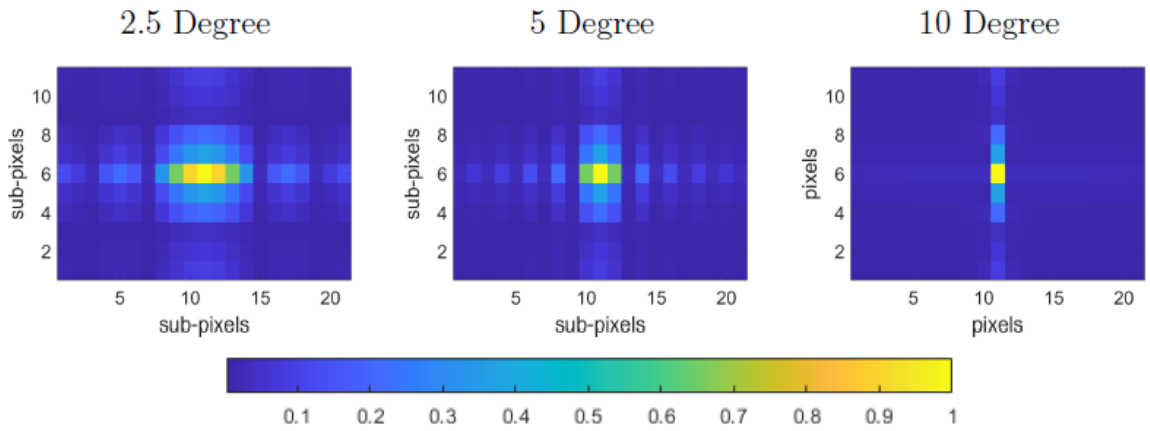

Figure 10: PSF for 2.5°, 5.0°, and 10° Apertures [3]

Sensing (DCPCS) model these imaging operators are referred to as $A_{M'}$ in (7) for each polarisation channel. In Chapter III a simplified version of a PSF was used in the evaluation of calibration errors. The next section will explore whether this substitution was valid.

4.2.2 Simplified Point Spread Function Comparison

In [3] Becker defines three different PSF's with a bandwidth of 622 MHz and aperture extents of 2.5°, 5.0°, and 10°. These three PSF's are shown in Figure 10. The robustness region found in [3] and shown in Figures 3 and 4 appeared consistent over a range of different imaging operators. Thus, it was decided to use a simplified PSF for computational efficiency in Chapter III. While conducting the Monte Carlo Simulations for the calibration error study, an error in the implementation of the ϵ setting code was discovered. The error in setting ϵ resulted in the constraint on the basis pursuit denoising (BPDN) problem in (4) being an order of magnitude larger than expected. The combination of using a new imaging operator and the different BPDN constraint led to a desire to want to verify the results from Becker's research are applicable.

Figures 11 and 13 reproduce the results, with incorrect ϵ, from [3] for 400 Monte

Carlo simulated random scenes at each crosstalk level, aperture extent, and 1% target density. Figure 11 shows the average relative error for each of the three PSF's. As the Aperture extent increases the relative recovery error decreases. Figure 13 shows the total number of trials that produce a recovery error $e_b \leq 0.1$.

Figure 12 shows the average relative recovery error for the PSF's of 2.5°, 5.0°, and 10° apertures and simplified PSF at 1% scene sparsity with the updated ϵ settings. Comparing Figures 12a through 12c to Figure 11, the effect of changing the ϵ value does not appear to have had a material difference on the relative recovery error of the scene or where the robustness region should be drawn. Design points 1, 3, and 4 all fall below the good recovery threshold of $e_b \leq 0.1$ with point 2 marginally above it. When using the corrected ϵ value the relative error on $\boldsymbol{b}$ was found for each of the four corners of the robustness region to be 0.058 at point 1, 0.126 at point 2, 0.044 at point 3, and 0.051 at point 4. Table 3 shows the comparison of e_b for each of the corners of the robustness region for the old and corrected ϵ. For each of the four corner points the corrected ϵ has led to an increase in the relative error on $\boldsymbol{b}$. The average increase in e_b across the four corner points is 34%.

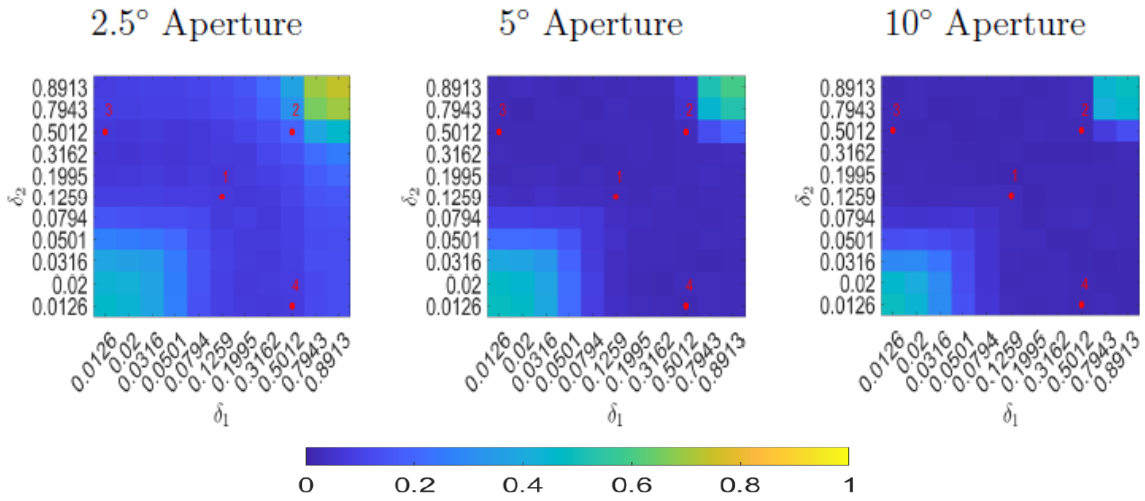

Figure 11: Average of relative recovery error e_b across Monte Carlo Simulations. Target Density levels of 1% [3]

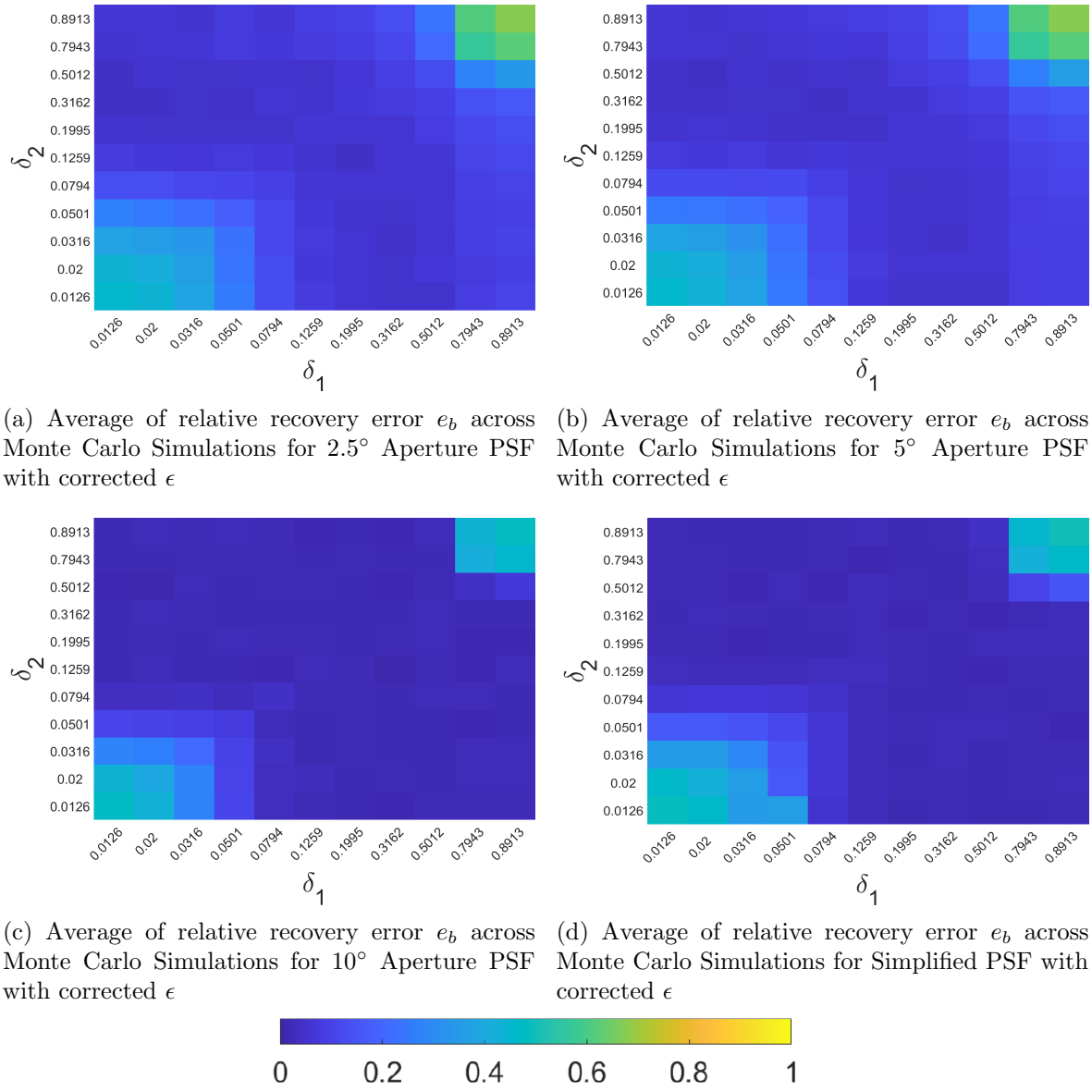

(a) Average of relative recovery error e_b across Monte Carlo Simulations for 2.5° Aperture PSF with corrected ϵ

(b) Average of relative recovery error e_b across Monte Carlo Simulations for 5° Aperture PSF with corrected ϵ

(c) Average of relative recovery error e_b across Monte Carlo Simulations for 10° Aperture PSF with corrected ϵ

(d) Average of relative recovery error e_b across Monte Carlo Simulations for Simplified PSF with corrected ϵ

Figure 12: Average of relative recovery error e_b across Monte Carlo Simulations for PSF's of 2.5°, 5.0°, and 10° Apertures and Simplified PSF at 1% Sparsity. Corrected ϵ value

Figure 14 shows the total success rate over 400 Simulations for PSF's of 2.5°, 5.0°, and 10° Apertures and Simplified PSF at 1% sparsity using the corrected ϵ. Similar to the relative error figures discussed above when comparing Figures 14a through 14c to Figure 13 there does not appear to be a material difference on the total number

Table 3: Comparison of e_b for old and corrected ϵ at 1% Sparsity

Pair #:	δ_1	δ_2	Old e_b	Corrected e_b	Percentage Change (%)
1	0.1259	0.1259	0.0448	0.0583	+30.1
2	0.5012	0.5012	0.0794	0.1259	+58.6
3	0.5012	0.0126	0.3081	0.0436	+14.4
4	0.0126	0.5012	0.0386	0.0513	+32.9

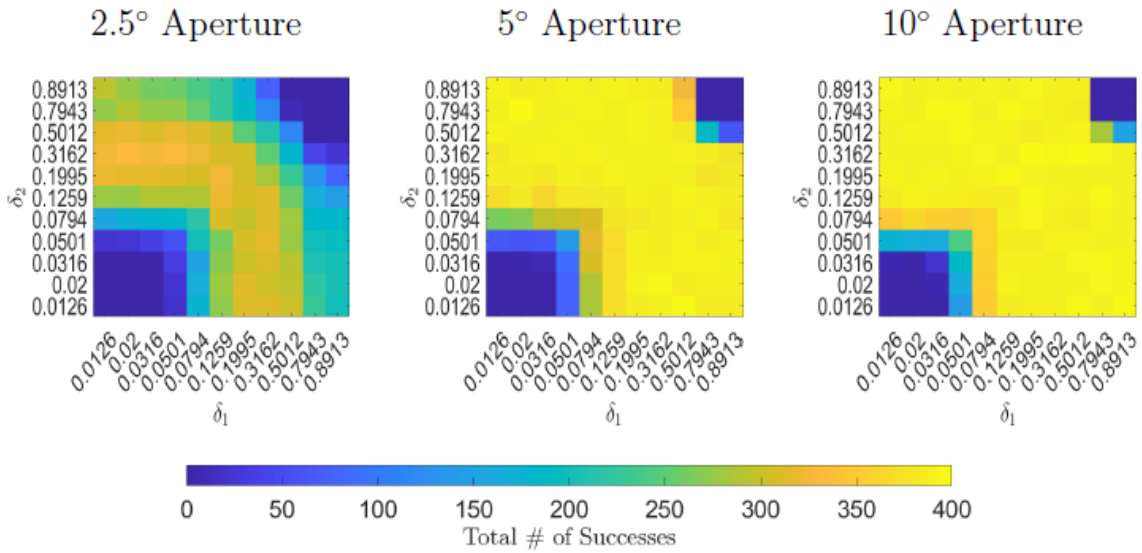

Figure 13: Total Success Rate of 400 Simulations for PSF's of 2.5°, 5.0°, and 10° Apertures at 1% Sparsity [3]

of successful trials at each design point. No material change in the success rate is what was expected when observing that the average relative error remained the same. When using the corrected ϵ value the success rate for each of the four corners of the robustness region was found to be 82.5% at point 1, 50.25% at point 2, 88.5% at point 3, and 85.25% at point 4. The minor growth in e_b has not translated to a corresponding decrease in the success rate. The lack of change to the success rate can be attributed to the mean relative error across the region still falling well below the 0.1 threshold.

In Figures 12 and 14 the results of the simplified PSF appear to closely mirror those of the 5° sub-aperture. On the surface the similarity of results seems strange as

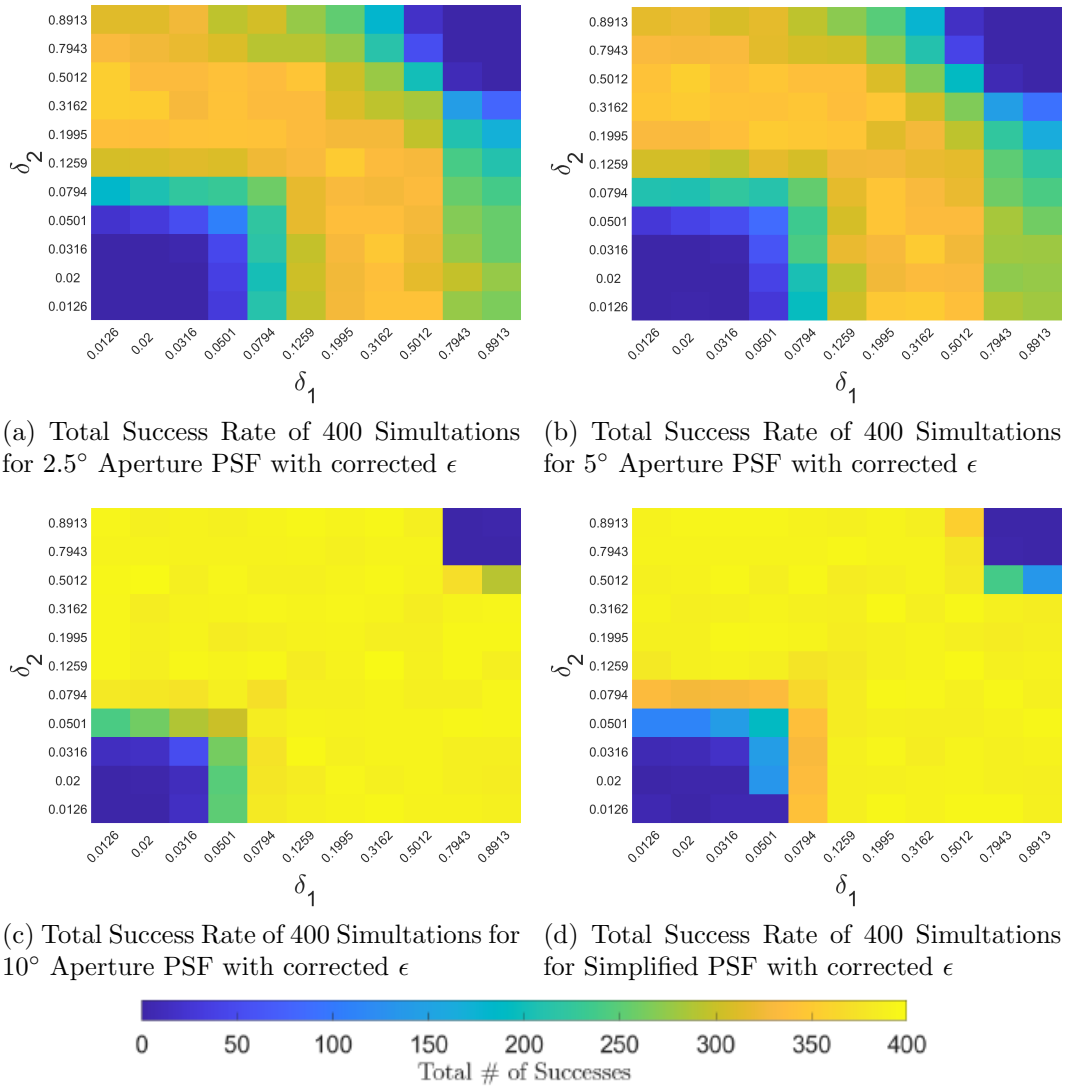

(a) Total Success Rate of 400 Simultations for 2.5° Aperture PSF with corrected ϵ

(b) Total Success Rate of 400 Simultations for 5° Aperture PSF with corrected ϵ

(c) Total Success Rate of 400 Simultations for 10° Aperture PSF with corrected ϵ

(d) Total Success Rate of 400 Simultations for Simplified PSF with corrected ϵ

Figure 14: Total Success Rate over 400 Simulations for PSF's of 2.5°, 5.0°, and 10° Apertures and Simplified PSF at 1% Sparsity. Corrected ϵ value

the 5° sub-aperture PSF has a much higher fidelity versus the 3×3 simplified PSF.

Figure 15 shows a comparison between the magnitudes of the center 3×3 points of the 2.5° sub-aperture PSF, 5° sub-aperture PSF, 10° sub-aperture PSF, and the simplified PSF. Comparing the simplified PSF to the other three PSFs, it is clear that the 5° sub-aperture PSF is visually the most similar. In the cross range direction the 5° sub-aperture PSF and the simplified PSF are almost identical. In the range

direction the 5° sub-aperture PSF has less energy than the simplified PSF, however on the whole the two PSF's are very similar. Looking at the complete 5° sub aperture PSF in Figure 10 it can be seen that there is much more energy in the outer range sidelobes versus the cross-range sidelobes which explains the observations in Figure 15.

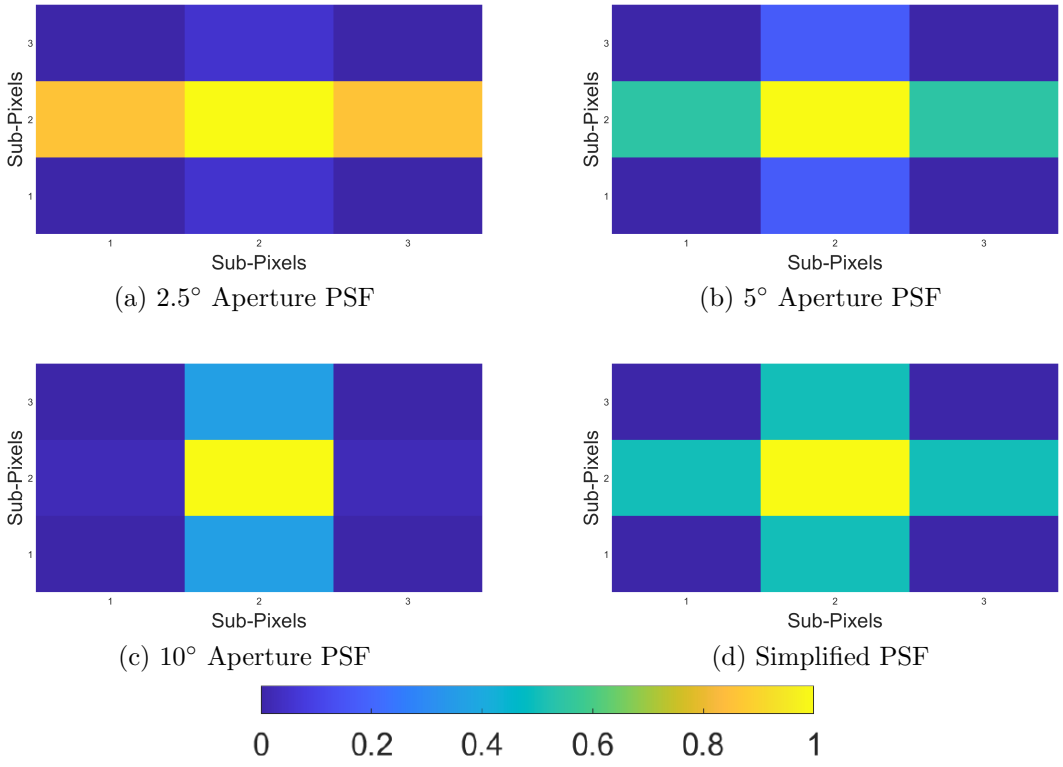

(a) 2.5° Aperture PSF

(b) 5° Aperture PSF

(c) 10° Aperture PSF

(d) Simplified PSF

Figure 15: Comparison of the centre of the 2.5° aperture PSF, 5° aperture PSF, 10° aperture PSF, and the simplified PSF

4.2.3 Conclusions

In conclusion through the comparison of the results in this section with those in [3] it appears that the error in ϵ setting in previous work was minor, representing a 34% increase in average recovery error across the four corners of the robustness region. This minor error therefore should not invalidate the results or conclusions from previous work.

The simplified PSF used in Chapter III and [1] takes on very similar characteristics as the centre of the 5° sub-aperture PSF used in [3]. The similarity between the simplified PSF and the 5° sub-aperture PSF can also be seen in the comparison of results of the total success rate and average relative recover error e_b with only a small difference in the results. The similarity in the two PSFs affirms that the substitution of the simplified PSF in Chapter III was valid.

4.3 Epsilon setting in Basis Pursuit Denoising

4.3.1 Section Overview

In the BPDN problem in (12) (repeated below) ϵ is a positive constant that is chosen to loosen the ℓ_2 constraint.

$$\hat{\boldsymbol{b}} = \arg\min_{\boldsymbol{b}} ||\boldsymbol{b}||_1 \text{ s.t. } ||\tilde{\boldsymbol{y}} - \boldsymbol{ADb}||_2 \leq \epsilon$$

In DCPCS the ϵ value is chosen in accordance with the characteristics of the imaged clutter [1]. The threshold of which represents the radius of a Gaussian Probability Density Function (PDF) spheroid in $M \times N$-dimensional space, or as colloquially referred to as an "Error Ball". This section will look at the math behind setting ϵ in a zero calibration error environment. We will then explore how the introduction of a

model mismatch drives the ϵ value to deviate from purely considering the expected image clutter.

4.3.2 Setting Epsilon without errors

The BPDN ℓ_2 constraint for solution estimate $\hat{b}$ in (12) is (Dr Julie Jackson, personal communication, October 2022)

$$||\tilde{\boldsymbol{y}} - \boldsymbol{ADb}||_2 \leq \epsilon. \tag{32}$$

If we substitute in (11) for our observed data we get

$$||\boldsymbol{AD}\tilde{\boldsymbol{b}} + \boldsymbol{Aw} - \boldsymbol{ADb}||_2 \leq \epsilon. \tag{33}$$

When $\hat{\boldsymbol{b}} = \boldsymbol{b}$, the imaged clutter term must satisfy

$$||\boldsymbol{Aw}||_2^2 \leq \epsilon^2. \tag{34}$$

In simulations knowledge of the clutter power is intrinsic in the model; however, for real world data an estimate for imaged clutter can be taken [45]. If we assume that clutter in each pixel is Independent and Identically Distributed (IID) complex Gaussian, then the imaged clutter $\tilde{\boldsymbol{w}}$ is a matrix $\boldsymbol{A}$ multiplied with a complex Gaussian vector $\boldsymbol{w}$ ($\tilde{\boldsymbol{w}} = \boldsymbol{Aw}$), which produces a complex Gaussian vector. According to Lancaster a chi-squared random variable is a sum of squares of independently distributed standard normal random variables [46]. A chi-squared random variable which is the

sum of k standard normal variables is said to have k Degrees of Freedom (DoF). Then the power of the imaged clutter,

$$||\tilde{\boldsymbol{w}}||_2^2 = \sum_{i=1}^{MN} |\tilde{\boldsymbol{w}}|^2 \tag{35}$$

is the sum of squares of $M \times N$ complex random variables, each with variance $\sigma_{\tilde{w}_i}^2$. In terms of unit normal Gaussian random variables, $n_i \sim \mathcal{CN}(0,1)$

$$||\tilde{\boldsymbol{w}}||_2^2 = \sum_{i=1}^{MN} \mathrm{Re}\{\tilde{\boldsymbol{w}}\}^2 + \mathrm{Im}\{\tilde{\boldsymbol{w}}\}^2 \tag{36}$$

$$= \sum_{i=1}^{MN} \frac{\sigma_{\tilde{w}_i}^2}{2} n_i^2 + \sum_{j=1}^{MN} \frac{\sigma_{\tilde{w}_j}^2}{2} n_j^2 \tag{37}$$

Supposing that $\sigma_{\tilde{w}_i}^2 \approx \sigma_{\tilde{w}}^2 \forall i, j$, then

$$||\tilde{\boldsymbol{w}}||_2^2 \approx \frac{\sigma_{\tilde{w}}^2}{2} \sum_{i=1}^{2MN} n_i^2, \tag{38}$$

and the sum term is chi-squared distributed with $2MN$ DoF. We seek to select the random variable value where the chi-squared distribution reaches a desired level γ, in this case when $\gamma = 0.95$. If we recall the definition of a Cumulative Distribution Function (CDF) for a random variable Z is defined as

$$F(z) = P[Z \leq z]. \tag{39}$$

From the BPDN constraint and (38)

$$P[||\tilde{\boldsymbol{w}}||_2 \leq \epsilon] = \gamma \tag{40}$$

$$P[||\tilde{\boldsymbol{w}}||_2^2 \leq \epsilon^2] = \gamma \tag{41}$$

$$P[\frac{\sigma_{\tilde{w}}^2}{2} \sum_{i=1}^{2MN} n_i^2 \leq \epsilon^2] = \gamma \tag{42}$$

$$P[\sum_{i=1}^{2MN} n_i^2 \leq 2\frac{\epsilon^2}{\sigma_{\tilde{w}}^2}] = \gamma. \tag{43}$$

If we then take the inverse CDF of (43)

$$2\frac{\epsilon^2}{\sigma_{\tilde{w}}^2} = F_{\chi^2,2MN}^{-1}(\gamma) \tag{44}$$

$$\epsilon = \sqrt{\frac{\sigma_{\tilde{w}}^2}{2MN} F_{\chi^2,2MN}^{-1}(\gamma)} \tag{45}$$

It remains to determine if the clutter variance in the image domain $\sigma_{\tilde{\boldsymbol{w}}}^2 \approx \sigma_{\tilde{\boldsymbol{w}}_{\boldsymbol{i}}}^2$. Since the clutter is zero mean,

$$\sigma_{\tilde{\boldsymbol{w}}_{\boldsymbol{i}}}^2 = E[|\tilde{\boldsymbol{w}}_{\boldsymbol{i}}|^2]. \tag{46}$$

Under a spatial ergodicity assumption that all clutter maps through the PSF the same way and that the clutter is dense enough that all image pixels end up with a similarly-distributed clutter,

$$\sigma^2_{\tilde{\boldsymbol{w}}_{\boldsymbol{i}}} = E[|\tilde{\boldsymbol{w}}_{\boldsymbol{i}}|^2] \approx \frac{1}{MN}\sum_{i+1}^{MN} |\tilde{\boldsymbol{w}}_{\boldsymbol{i}}|^2 \tag{47}$$

$$\approx \frac{1}{MN}\sum_{i+1}^{MN} |[\boldsymbol{A}\boldsymbol{w}]_i|^2 \tag{48}$$

$$\approx \sigma_{\tilde{\boldsymbol{w}}}. \tag{49}$$

Thus, without any error present ϵ is set as

$$\epsilon = \sqrt{\frac{F^{-1}_{\chi^2,2MN}(\gamma)}{2MN}\sum_{i=1}^{MN} |[\boldsymbol{A}\boldsymbol{w}]_i|^2} \tag{50}$$

4.3.3 Setting Epsilon with calibration errors

If there are calibration errors in the radar system, the measured crosstalk matrix $\hat{\boldsymbol{C}}$ is the true antenna crosstalk $\boldsymbol{C}$ plus calibration error $\boldsymbol{C_e}$

$$\hat{\boldsymbol{C}} = \boldsymbol{C} + \boldsymbol{C_e}. \tag{51}$$

As shown in Section 3.3 in (28) the errors of each calibration measurement is distributed as $\sim \mathcal{CN}(0, \sigma^2_{\text{err}})$. Due to normalisation of each of the rows in the individual antenna crosstalk matrices and the kronecker products of these terms, the elements within $\boldsymbol{C_e}$ are not distributed as $\sim \mathcal{CN}(0, \sigma^2_{\text{err}})$. $\boldsymbol{C_e}$ is the driver of a model mismatch $\boldsymbol{A} - \hat{\boldsymbol{A}}$. Therefore ℓ_2 fit is impaired by both the measured clutter $\boldsymbol{A}\boldsymbol{w}$ and model mismatch $\boldsymbol{A} - \hat{\boldsymbol{A}}$:

$$||\tilde{\boldsymbol{y}} - \hat{\boldsymbol{A}}\boldsymbol{D}\boldsymbol{b}||_2 \leq \epsilon \tag{52}$$

$$||(\boldsymbol{A} - \hat{\boldsymbol{A}})\boldsymbol{D}\boldsymbol{b} + \boldsymbol{A}\boldsymbol{w}||_2 \leq \epsilon. \tag{53}$$

By the triangle inequality,

$$||(\boldsymbol{A} - \hat{\boldsymbol{A}})\boldsymbol{D}\boldsymbol{b} + \boldsymbol{A}\boldsymbol{w}||_2 \leq ||(\boldsymbol{A} - \hat{\boldsymbol{A}})\boldsymbol{D}\boldsymbol{b}||_2 + ||\boldsymbol{A}\boldsymbol{w}||_2 \tag{54}$$

The right hand side of the triangle inequality is not required to be less than ϵ, but defining an ϵ based on the right hand side of the triangle inequality is convenient and will probabilistically guarantee the residual error is less than the defined constraint variable, γ. Thus, we seek to find ϵ such that

$$P[||\boldsymbol{A}\boldsymbol{w}||_2 + ||(\boldsymbol{A} - \hat{\boldsymbol{A}})\boldsymbol{D}\boldsymbol{b}||_2 \leq \epsilon] = \gamma \tag{55}$$

A convenient approximation is to ensure

$$P[||\boldsymbol{A}\boldsymbol{w}||_2 \leq \epsilon_1] = \gamma \tag{56}$$

and

$$P[||(\boldsymbol{A} - \hat{\boldsymbol{A}})\boldsymbol{D}\boldsymbol{b}||_2 \leq \epsilon_2] = \gamma \tag{57}$$

hold. Then let $\epsilon = \epsilon_1 + \epsilon_2$. The ϵ_1 term should be set as outlined in Section 4.3.2.

The ϵ_2 can be set similarly, but $||(\boldsymbol{A} - \hat{\boldsymbol{A}})\boldsymbol{Db}||_2$ will need to be estimated for various sparsity levels and levels of calibration error.

Due to the complex interactions of the calibration errors with the true antenna parameters a numerical approach to estimating the value of ϵ_2 was not deemed practical. Instead, we decided to look at the ratio of residual error due to the model mismatch $|\boldsymbol{ADb}|$ and the imaged clutter $|\boldsymbol{Aw}|$ as a function of sparsity. Figures 16 and 17 show that even at the lowest values of calibration error the residual error due to model mismatch is twice as large as that caused by the imaged clutter. As expected, as the scene becomes less sparse the ratio between the model mismatch and the imaged clutter increases. Figures 16 and 17 also appear to show that the ratio of residual error due to model mismatch and imaged clutter does not vary for either the monostatic or dual antenna case.

With the ratio of $\frac{|\boldsymbol{AeDb}|}{|\boldsymbol{Aw}|} \geq 2$ for a $\sigma^2_{err} = 0.001$ indicating that the ϵ value is being over constrained. If we infer that $\epsilon_2 = 2\epsilon_1$ then it appears ϵ should be set at least three times higher for when sparsity is at 1%. If from Figures 16 and 17 we select

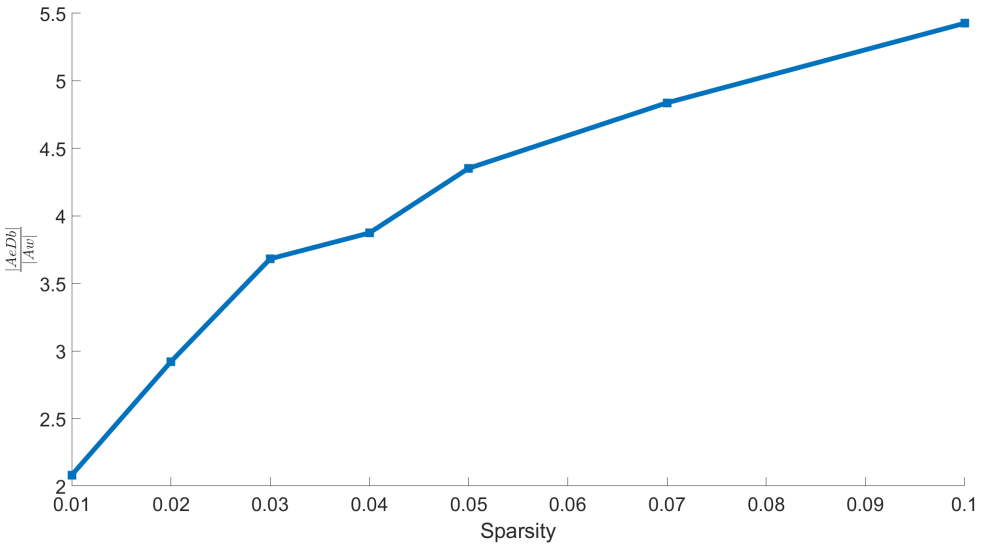

Figure 16: Ratio of model mismatch to imaged clutter against sparsity for $\sigma^2_{err} = 0.001$ for $\boldsymbol{C} = \boldsymbol{T}_2 \otimes \boldsymbol{T}_2^T$

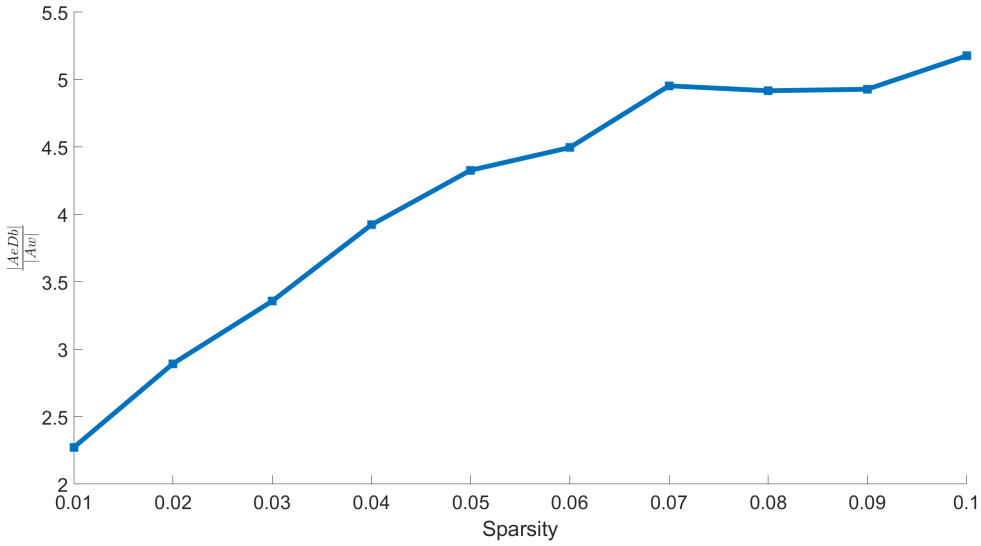

Figure 17: Ratio of model mismatch to imaged clutter against sparsity for $\sigma^2_{err} = 0.001$ for $\boldsymbol{C} = \boldsymbol{T}_{Jackson} \otimes \boldsymbol{R}^T_{Jackson}$

$\epsilon_2 = 4\epsilon_1$ which is approximately the ratio for sparsities up to about 5%, the results are shown in Figure 18.

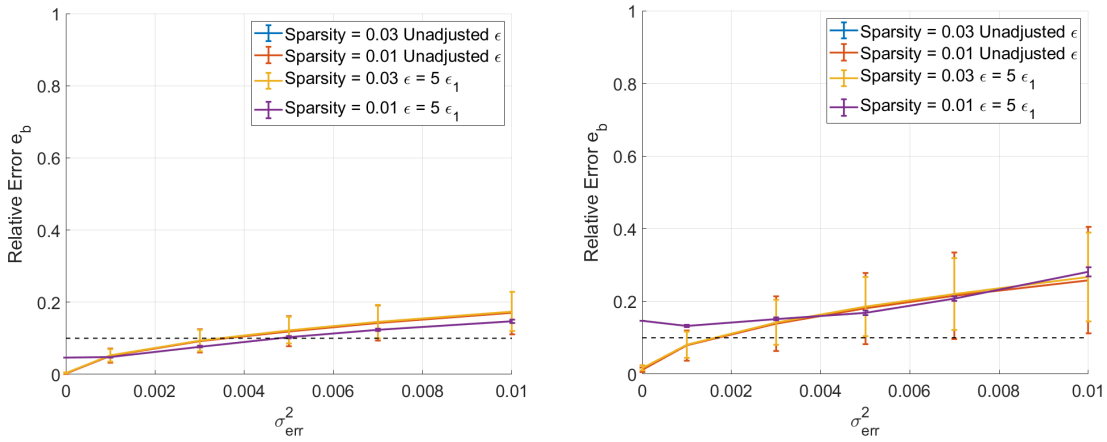

(a) $\boldsymbol{C} = \boldsymbol{T}_{Jackson} \otimes \boldsymbol{R}^T_{Jackson}$ (b) $\boldsymbol{C} = \boldsymbol{T}_2 \otimes \boldsymbol{T}_2^T$

Figure 18: Median relative error versus calibration error σ_e^2 for SCR = 40dB and HH channel dropped for crosstalks $\boldsymbol{C} = \boldsymbol{T_{Jackson}} \otimes \boldsymbol{R^T_{Jackson}}$ and $\boldsymbol{C} = \boldsymbol{T_2} \otimes \boldsymbol{T_2^2}$. Unadjusted ϵ and $\epsilon = 5\epsilon_1$. Error bars indicate the 10th and 90th percentiles.

Figure 18 contrasts the relative error versus calibration error for when ϵ is left

unadjusted or set to be five times the imaged clutter alone for the crosstalk matrices in (22) and (26). For small σ_{err}^2 values the adjusted $\epsilon = 5\epsilon_1$ mean relative error is greater than the unadjusted case. The worse recovery performance is likely due to the over relaxation of ϵ as Figures 16 and 17 show that $\epsilon = 3\epsilon_1$ would be a more appropriate fit. As the calibration error increases the $\epsilon = 5\epsilon_1$ matches closely with the unadjusted line. An interesting observation is the relaxed ϵ appears to have greatly reduced the size of the error bars for the 1% sparsity case. At 3% sparsity, the adjusted $\epsilon = 5\epsilon_1$ adjusted curve falls exactly over the unadjusted curve.

4.3.4 Conclusions

In this section we have shown that in a zero calibration error environment it is possible to set the BPDN constant ϵ to meet a given "error ball" probability predicted by imaged clutter, as outlined in (50). However, in the presence of calibration error, which produces a model mismatch, the residual error of the ℓ_2 norm of the BPDN equation is very quickly dominated by model mismatch. Adjusting the ϵ value to loosen the constraint does not appear to have an appreciable beneficial impact on relative recovery error e_b.

V. Conclusions

5.1 Key Conclusions

The addition of polarimetry to Synthetic Aperture Radar (SAR) has the affect that more information about the scene can be collected, with the trade-off of extra data that requires processing, storage, and transmission. Dropped-Channel PolSAR Compressive Sensing (DCPCS) provides a method to reduce the amount of data required to be collected without sacrificing the additional information. Previous research on DCPCS defining the required antenna crosstalk levels and constructing a prototype antenna for a DCPCS system. **The goal of this research was to determine the required calibration accuracy of the antenna system in order for DCPCS to be successful. In addition, this thesis looked at the importance of properly setting the basis pursuit denoising (BPDN) threshold in accordance with the expected clutter and calibration error levels.**

In Chapter III, a Gaussian calibration error was added to a range of different crosstalk matrices representing the corners of Becker's robustness region representing a monostatic radar, as well as a pair of antennas with different transmit and receive characteristics. It was shown that a radar calibration accuracy on the order of -25 dB or better is needed for successful recover using BPDN for DCPCS in a single antenna system. However, this is room for improvement with the use of different antennas for transmit and receive improving recovery.

In Chapter IV, the robustness region of a simplified Point Spread Function (PSF) was verified to be the same as the one discussed by Becker. By showing that the simplified PSF has the same robustness region as the more complex PSF's used in Becker's work the validity of the results in Chapter III were confirmed. Being able to use a simplified PSF in place of a more detailed imaging operator allows for quicker

trials to be conducted during future DCPCS studies. Chapter IV also shows the proper way to set ϵ in accordance with the expected clutter levels.

5.2 Significance of the Research

Using the results from Chapters III and IV, DCPCS has been shown to have a significant reliance on the accuracy of calibration equipment both in terms of ϵ setting and scene recovery. Identification of the importance of this relationship has the potential to direct future studies in the direction of possible self-calibration signal processing techniques. With a correctly designed high-crosstalk antenna the results in Chapter III show that it should be possible to have successful scene recovery at 3% sparsity for a monostatic system and even higher for a system with different receive and transmit antennas.

5.3 Future Studies

The results of this study could be extended by:

- Extending the simulations from this work to include extended scatterers or real world data such as that provided by the GOTCHA Data Set.
- Extending the study of crosstalk robustness regions past the monostatic assumption to include transmit and receive antennas with different crosstalk characteristics.
- Investigation into whether self-calibration techniques that can estimate the unknowns in the $\boldsymbol{A}$ matrix in addition to estimating $\boldsymbol{b}$ can account for some calibration errors and loosen the requirements on calibration measurement accuracy.

- Collect laboratory measurements using different crosstalk antennas to verify simulated results for monostatic radar systems.

Bibliography

1. Julie Ann Jackson and Forest Lee-Elkin. Exploiting Channel Crosstalk for Polarimetric SAR Compressive Sensing. *IEEE Transactions on Aerospace and Electronic Systems*, Vol 56: pages 475–485, 2020.

2. Julie Ann Jackson and Forest Lee-Elkin. System, method, and apparatus for recovering polarization radar data, United States of America Patent US11194104B1, Dec. 2021.

3. John Becker. Theory and design of a highly compressed dropped-channel polarimetric synthetic aperture radar. Ph.D. Dissertation, Air Force Institute of Technology, 2022.

4. John Becker, Julie Ann Jackson, and Jeffrey Massman. Crosstalk is good: Antenna design to enable polarimetric compressive sensing. Antenna Measurement Techniques Association Symposium, Oct 2022.

5. Ian Faulconbridge. *Radar Fundamentals*. Argos Press, 1st edition, 2002.

6. Carl A Wiley. Synthetic aperture radars. *IEEE Transactions on Aerospace and Electronic Systems*, (3): pages 440–443, 1985.

7. Charles V. Jakowatz, Daniel E. Wahl, Paul H. Eichel, Dennis C. Ghiglia, and Paul A. Thompson. *Spotlight-Mode Synthetic Aperture Radar: A Signal Processing Approach*. Springer US, 1996.

8. Mark A Richards, Jim Scheer, William A Holm, and William L Melvin, editors. *Principles of modern radar*. SciTech Publishing, Edison, NJ, 2010.

9. Ricardo Rendon Cepeda. Applications of synthetic aperture radar satellites to environmental monitoring, Nov 2020. https://www.csis.org/blogs/technology-policy-blog/applications-synthetic-aperture-radar-satellites-environmental.

10. Yan Wang, Jing-wen Li, Bing Sun, and Jie Chen. Airborne geographically referenced stripmap SAR data processing. In *2014 IEEE Geoscience and Remote Sensing Symposium*, pages 620–623, 2014.

11. Hyung-Sup Jung, Lei Zhang, and Sang-Hoon Hong. Advanced sensor technologies in geospatial sciences and engineering. Hindawi, 2019.

12. J.A. Jackson and F. Lee-Elkin. Relating phenomenology to measurement matrix for dropped channel polarimetric SAR. In *NATO STO-MP-SET-265 Meeting Proceedings*, pages MP–SET–265–12, 2019.

13. John Becker and Julie Ann Jackson. Super-resolution using dropped-channel PolSAR compressive sensing. *IEEE Radar Conference*, pages 1–6, 2019.

14. Jacob Morrison, Julie Ann Jackson, and John Becker. Robustness of PolSAR CS to calibration error. IEEE Radar Conference, May 2023.

15. M.D. Desai and W.K. Jenkins. Convolution backprojection image reconstruction for spotlight mode synthetic aperture radar. *IEEE Transactions on Image Processing*, Vol 1(4): pages 505–517, 1992.

16. Xinhua Mao, Daiyin Zhu, and Zhaoda Zhu. Autofocus correction of APE and residual RCM in spotlight SAR polar format imagery. *IEEE Transactions on Aerospace and Electronic Systems*, Vol 49(4): pages 2693–2706, 2013.

17. Chu He, Qian Feng, Ming Liu, Xiaonian Liu, and Mingsheng Liao. Learning based decomposition for polarmetric SAR images. In *2011 IEEE International Geoscience and Remote Sensing Symposium*, pages 452–455, 2011.

18. S. R. Cloude. *Polarisation: applications in remote sensing*. Oxford University Press, 2010.

19. D.L. Donoho. Compressed sensing. *IEEE Transactions on Information Theory*, Vol 52(4): pages 1289–1306, 2006.

20. C.E. Shannon. Communication in the presence of noise. *Proceedings of the IRE*, Vol 37(1): pages 10–21, 1949.

21. Richard G. Baraniuk. Compressive sensing [lecture notes]. *IEEE Signal Processing Magazine*, 24(4): pages 118–121, 2007.

22. Simon Foucart and Holger Rauhut. An invitation to compressive sensing. In *A mathematical introduction to compressive sensing*, pages 1–39. Springer, 2013.

23. Huizhang Yang, Chengzhi Chen, Shengyao Chen, and Feng Xi. Sub-Nyquist SAR via quadrature compressive sampling with independent measurements. *Remote Sensing*, Vol 11(4): pages 472, 2019.

24. Vishal M. Patel, Glenn R. Easley, Dennis M. Healy, and Rama Chellappa. Compressed synthetic aperture radar. *IEEE Journal on Selected Topics in Signal Processing*, Vol 4: pages 244–254, Apr 2010.

25. Moshe Mishali and Yonina C. Eldar. *Xampling: compressed sensing of analog signals*, page 88–147. Cambridge University Press, 2012.

26. Kfir Aberman and Yonina C. Eldar. Sub-nyquist SAR via Fourier domain range-doppler processing. *IEEE Transactions on Geoscience and Remote Sensing*, Vol 55: pages 6228–6244, Nov 2017.

27. Huizhang Yang, Shengyao Chen, Feng Xi, and Zhong Liu. Quadrature compressive sampling SAR imaging. In *IGARSS 2018 - 2018 IEEE International Geoscience and Remote Sensing Symposium*, pages 5847–5850, 2018.

28. Qilian Liang. Compressive sensing for synthetic aperture radar in fast-time and slow-time domains. In *Asilomar Conference on Signals, Systems and Computers*, pages 1479–1483, 2011.

29. John Becker and Julie Ann Jackson. Expansion of dropped-channel PolSAR CS to include a spatial dictionary. *5th Int'l Workshop on Compressed Sensing applied to Radar, Multimodal Sensing, and Imaging (CoSeRa)*, 2018.

30. Curtis H Casteel Jr, LeRoy A Gorham, Michael J Minardi, Steven M Scarborough, Kiranmai D Naidu, and Uttam K Majumder. A challenge problem for 2D/3D imaging of targets from a volumetric data set in an urban environment. In *Algorithms for Synthetic Aperture Radar Imagery XIV*, volume 6568, pages 97–103. SPIE, 2007.

31. Anthony Freeman, Yuhsyen Shen, and Charles L Werner. Polarimetric SAR calibration experiment using active radar calibrators. *IEEE Transactions on geoscience and remote sensing*, Vol 28(2): pages 224–240, 1990.

32. Werner Schaefer. Antenna parameters and antenna calibration. `https://incompliancemag.com/article/antenna-parameters-and-antenna-calibration/`, Jun 2016.

33. American national standard for electromagnetic compatibility–radiated emission measurements in electromagnetic interference (EMI) control–calibration and qualification of antennas (9 kHz to 40 GHz). *ANSI C63.5-2017 (Revision of ANSI C63.5-2005)*, pages 1–114, 2017.

34. M. Kai, F. Hou, and D. Sun. Design of a broadband dual-polarized mircostrip antenna array with high isolation. In *Sixth Asia-Pacific Conf. on Antennas and Propagation (APCAP)*, pages 1–3, October 2017.

35. R. Touzi, P. W. Vachon, and J. Wolfe. Requirement on Antenna Cross-Polarization Isolation for the Operational Use of C-Band SAR Constellations in Maritime Surveillance. *IEEE Geoscience and Remote Sensing Letters*, Vol 7(4): pages 861–865, Oct 2010.

36. P.D. Patel. A dual polarised microstrip antenna with low cross-polarisation, for SAR applications. In *IEEE Antennas and Propagation Society Int'l Symposium*, volume 3, pages 1536–1539, Jul 1996.

37. K. Sarabandi, F. T. Ulaby, and M. A. Tassoudji. Calibration of polarimetric radar systems with good polarization isolation. *IEEE Trans. on Geoscience and Remote Sensing*, Vol 28(1): pages 70–75, jan 1990.

38. Virendra Kumar, Rakesh Kumar Verma, U. S. Pandey, K. S. Beenamole, and Ravi Kumar Gangwar. Thermal equilibrium in t/r module operation and active phased array antenna calibration. In *2021 IEEE MTT-S International Microwave and RF Conference (IMARC)*, pages 1–4, 2021.

39. Howard A. Zebker, Jakob J. Van Zyl, Stephen L. Durden, and Lynne Norikane. Calibrated imaging radar polarimetry: Technique, examples, and applications. *IEEE Trans. on Geoscience and Remote Sensing*, Vol 29: pages 942–961, Nov 1991.

40. E. van den Berg and M. P. Friedlander. SPGL1: A solver for large-scale sparse reconstruction, Dec 2019. https://friedlander.io/spgl1.

41. E. van den Berg and M. P. Friedlander. Probing the pareto frontier for basis pursuit solutions. *SIAM Journal on Scientific Computing*, Vol 31(2): pages 890–912, 2008.

42. Shuyang Ling and Thomas Strohmer. Self-calibration and bilinear inverse problems via linear least squares. *SIAM Journal on Imaging Sciences*, Vol 11(1): pages 252–292, 2018.

43. Jason T. Parker. Approximate message passing algorithms for generalized bilinear inference. Ph.D. Dissertation, The Ohio State University, 2014.

44. Xiao Dong and Yunhua Zhang. A novel compressive sensing algorithm for SAR imaging. *IEEE Journal of Selected Topics in Applied Earth Observations and Remote Sensing*, 7(2): pages 708–720, 2014.

45. Hui Tang, Xianrong Wan, and Henyu Ke. Detection of a well-characterized signal in persistent clutter. In *2016 CIE International Conference on Radar (RADAR)*, pages 1–4, 2016.

46. Henry Oliver Lancaster and Eugene Seneta. Chi-square distribution. *Encyclopedia of biostatistics*, Vol 2, 2005.

Acronyms

ADC analogue-to-digital conversion. 9, 10

AFRL Air Force Research Laboratory. 13

BP basis pursuit. 8

BPDN basis pursuit denoising. iv, 1, 2, 8, 12, 13, 14, 16, 18, 21, 22, 23, 24, 25, 31, 33, 39, 40, 41, 47, 48, 1

CDF Cumulative Distribution Function. 41, 42

CS Compressive Sensing. 1, 3, 7, 8, 9, 10, 12, 13, 14

DCPCS Dropped-Channel PolSAR Compressive Sensing. iv, 1, 2, 10, 13, 14, 16, 18, 22, 24, 31, 32, 39, 48, 49, 1

DoF Degrees of Freedom. 41

EM Electromagnetic. 3

EMI Electromagentic Interference. 17

IID Independent and Identically Distributed. 40

MRI Magnetic Resonance Imaging. 7

PDF Probability Density Function. 39

PFA Polar Format Algorthm. 5

PolSAR Polarimetric Synthetic Aperture Radar. 1, 3, 4, 6, 7, 10

PSF Point Spread Function. 24, 25, 26, 32, 33, 36, 37, 38, 39, 42, 48

SAR Synthetic Aperture Radar. 1, 3, 4, 5, 7, 8, 9, 10, 13, 32, 48

SCR Signal-to-Clutter Ratio. 26, 27

SWaP-C Size, Weight, Power, and Cooling. 3

REPORT DOCUMENTATION PAGE

Form Approved
OMB No. 0704–0188

The public reporting burden for this collection of information is estimated to average 1 hour per response, including the time for reviewing instructions, searching existing data sources, gathering and maintaining the data needed, and completing and reviewing the collection of information. Send comments regarding this burden estimate or any other aspect of this collection of information, including suggestions for reducing this burden to Department of Defense, Washington Headquarters Services, Directorate for Information Operations and Reports (0704–0188), 1215 Jefferson Davis Highway, Suite 1204, Arlington, VA 22202–4302. Respondents should be aware that notwithstanding any other provision of law, no person shall be subject to any penalty for failing to comply with a collection of information if it does not display a currently valid OMB control number. **PLEASE DO NOT RETURN YOUR FORM TO THE ABOVE ADDRESS.**

1. REPORT DATE *(DD–MM–YYYY)*	2. REPORT TYPE	3. DATES COVERED *(From — To)*
23–03–2023	Master's Thesis	Sept 2021 — Mar 2023

4. TITLE AND SUBTITLE

Effects of Calibration Errors on Dropped-Channel Polarimetric Synthetic Aperture Radar

5a. CONTRACT NUMBER

5b. GRANT NUMBER

5c. PROGRAM ELEMENT NUMBER

6. AUTHOR(S)

FLTLT Jacob C. Morrison

5d. PROJECT NUMBER

5e. TASK NUMBER

5f. WORK UNIT NUMBER

7. PERFORMING ORGANIZATION NAME(S) AND ADDRESS(ES)

Air Force Institute of Technology
Graduate School of Engineering and Management (AFIT/EN)
2950 Hobson Way
WPAFB OH 45433-7765

8. PERFORMING ORGANIZATION REPORT NUMBER

AFIT-ENG-MS-23-M-049

9. SPONSORING / MONITORING AGENCY NAME(S) AND ADDRESS(ES)

Left Intentionally Blank

10. SPONSOR/MONITOR'S ACRONYM(S)

11. SPONSOR/MONITOR'S REPORT NUMBER(S)

12. DISTRIBUTION / AVAILABILITY STATEMENT

DISTRIBUTION STATEMENT A:
APPROVED FOR PUBLIC RELEASE; DISTRIBUTION UNLIMITED.

13. SUPPLEMENTARY NOTES

14. ABSTRACT

Compressed Sensing (CS) is a mathematical technique that can be applied to sparse data sets to allow for sub-Nyquist sampling. DCPCS is a CS technique that recovers the signal from unmeasured polarisation channels due to antenna crosstalk coupling the information onto the remaining channels. DCPCS reduces data storage/transmission and receiver hardware requirements. This thesis examines the robustness of DCPCS to calibration errors on the antenna crosstalk matrix. Although the antenna design problem is relaxed to a large region of acceptable crosstalk values, very accurate calibration may be required in a monostatic radar. This thesis also looks at the importance of properly setting the BPDN threshold ϵ in accordance with the expected clutter and calibration error levels, showing that without any model mismatches it is possible to accurately set ϵ using the estimated scene clutter. Finally, the validity of using a simplified Point Spread Function (PSF) imaging operator to reduce the computational complexity of simulations is shown.

15. SUBJECT TERMS

Polarimetric Radar, Compressive Sensing, Dropped-Channel Polarimetric Compressive Sensing

16. SECURITY CLASSIFICATION OF:			17. LIMITATION OF ABSTRACT	18. NUMBER OF PAGES	19a. NAME OF RESPONSIBLE PERSON
a. REPORT	b. ABSTRACT	c. THIS PAGE			Dr Julie A. Jackson, AFIT/ENG
U	U	U	UU	69	19b. TELEPHONE NUMBER *(include area code)* (937) 255-3636, x4678; julie.jackson@afit.edu